Structural basis for ion selectivity in TMEM175 K+ channels

Brunner, Janine D ; Jakob, Roman P ; Schulze, Tobias ; Neldner, Yvonne ; Moroni, Anna ; Thiel, Gerhard ; Maier, Timm ; Schenck, Stephan

Abstract: The TMEM175 family constitutes recently discovered K+ channels that are important for autophagosome turnover and lysosomal pH regulation and are associated with the early onset of Parkinson Disease. TMEM175 channels lack a P-loop selectivity filter, a hallmark of all known K+ channels, raising the question how selectivity is achieved. Here, we report the X-ray structure of a closed bacterial TMEM175 channel in complex with a nanobody fusion-protein disclosing bound K+ ions. Our analysis revealed that a highly conserved layer of threonine residues in the pore conveys a basal K+ selectivity. An additional layer comprising two serines in human TMEM175 increases selectivity further and renders this channel sensitive to 4-aminopyridine and Zn2+. Our findings suggest that large hydrophobic side chains occlude the pore, forming a physical gate, and that channel opening by iris-like motions simultaneously relocates the gate and exposes the otherwise concealed selectivity filter to the pore lumen.

DOI: https://doi.org/10.7554/eLife.53683

Title: Structural basis for ion selectivity in TMEM175 K^+ channels

Authors: Janine D. Brunner[1,2,3,4,5]*, Roman P. Jakob[2]†, Tobias Schulze[6]†, Yvonne Neldner[1]§, Anna Moroni[7], Gerhard Thiel[6], Timm Maier[2], Stephan Schenck[1,3,4,5]*

Affiliations:

[1]Department of Biochemistry, University of Zürich, Winterthurerstrasse 190, 8057 Zürich, Switzerland.

[2]Department Biozentrum, University of Basel, Klingelbergstrasse 50/70, 4056 Basel, Switzerland.

[3]Laboratory of Biomolecular Research, Paul Scherrer Institut, CH-5232 Villigen-PSI, Switzerland.

[4]VIB-VUB Center for Structural Biology, VIB, Brussels, Belgium.

[5]Structural Biology Brussels, Vrije Universiteit Brussel, Brussels, Belgium.

[6]Membrane Biophysics, Technical University of Darmstadt, Darmstadt, Germany.

[7]Department of Biosciences, University of Milano, Italy.

§Present address: Department of Trauma, University Hospital Zürich, Sternwartstrasse 14, 8091 Zürich, Switzerland

*Correspondence to: janine.brunner@vub.be (J.D.B); stephan.schenck@vub.be (S.S.)

†These authors contributed equally to the work.

Abstract: The TMEM175 family constitutes recently discovered K^+ channels that are important for autophagosome turnover and lysosomal pH regulation and are associated with the early onset of Parkinson Disease. TMEM175 channels lack a P-loop selectivity filter, a hallmark of all known K^+ channels, raising the question how selectivity is achieved. Here, we report the X-ray structure of a closed bacterial TMEM175 channel in complex with a nanobody fusion-protein disclosing bound K^+ ions. Our analysis revealed that a highly conserved layer of threonine residues in the pore conveys a basal K^+ selectivity. An additional layer comprising two serines in human TMEM175 increases selectivity further and renders this channel sensitive to 4-aminopyridine and Zn^{2+}. Our findings suggest that large hydrophobic side chains occlude the pore, forming a physical gate, and that channel opening by iris-like motions simultaneously relocates the gate and exposes the otherwise concealed selectivity filter to the pore lumen.

Introduction

Potassium is the major intracellular cation and crucial to many fundamental cellular processes such as maintenance of the resting membrane potential, repolarization of action potentials, counter-ion flux and osmoregulation. The function and distribution of K^+ ions in endomembrane compartments such as endosomes and lysosomes are less clear and their significance is only recently beginning to emerge [1]. Lysosomes, the recycling organelles of the cell, are characterized by a very low luminal pH for the efficient decomposition of its contents. They have been recognized lately as a central hub in metabolic regulation of the cell [2,3]. Like in other endomembrane compartments, ion channels and transporters, in conjunction with the vacuolar-type ATPase, are essential for the regulation of the luminal pH, the membrane potential and organelle fusion and thus regulate the transport of other solutes across the membrane and also the dynamics and fate of these organelles [4]. It has been known for decades that lysosomal membranes are permeable for K^+ and even more so for Cs^+, a hallmark of this type of endo-membranes [5]. The underlying channel has recently been identified as a member of the transmembrane protein family 175 (TMEM175). The TMEM175 channel was found to mediate a major K^+ permeability of lysosomes and late endosomes (hence also named K_{EL}) [6], and is not related to canonical K^+ channels. TMEM175 channels are present in animals, eubacteria and archaea but are not found in plants and fungi. They exhibit selectivities ranging from P_{Cs}/P_{Na} of ~20 in vertebrates to P_K/P_{Na} of ~2-5 in bacteria and have been described as 'leak-like' channels [6]. TMEM175 channels, unlike canonical K^+ channels, conduct Cs^+ ions and are not blocked by Ba^{2+}, tetraethylammonium or quinine but instead by Zn^{2+} ions. Like other K^+ channels, they are blocked by 4-aminopyridine (with the exception of bacterial TMEM175 proteins), and conduct Rb^+ but not Ca^{2+} and N-methyl-D-glucamine [6]. The vertebrate TMEM175 proteins are composed of two homologous non-identical repeats, each comprising six transmembrane domains forming dimers; the bacterial homologues consist of only one such repeat and form tetramers [6,7]. In prokaryotes, the function of TMEM175 proteins is currently unclear but may be linked to the regulation of the membrane potential [6]. In vertebrates, deletion of the TMEM175 gene leads to increased lysosomal pH under conditions of starvation, reduced proteolytic activity in lysosomes and aberrant autophagosome fusion and clearance [6,8]. The human TMEM175 channel has been linked to Parkinson disease (PD) by several genome wide association studies and is considered as a highly significant risk gene for the early onset of this neurodegenerative disease [8-10]. The

deficiency in autophagosome clearance and the impaired proteolytic activity by loss of TMEM175 are presumably causative for the accumulation of insoluble α-synuclein fibrils in PD models and could explain why this channel is relevant for the progression of PD [8]. In particular with its channel function, TMEM175 may thus be a viable drug-target to interfere with the pathogenesis.

Selectivity for K^+ ions, with the exception of the very weakly selective trimeric intracellular cation (TRIC) channels [11], is intimately associated with a P-loop architecture [12]. The lack of such a P-loop motif in TMEM175 channels hence raises the question how K^+ conduction and selectivity is achieved in this unrelated architecture. To gain insight into the structure and mechanisms of this new family of ion channels we structurally characterized a bacterial TMEM175 member. We obtained a crystal structure at a resolution of 2.4 Å of a TMEM175 channel from *Marivirga tractuosa* (MtTMEM175) and in combination with functional analysis, propose how selectivity for K^+ ions is achieved. We further provide data that explains the increased potassium selectivity as well as the pronounced sensitivity towards 4-aminopyridine and zinc of human TMEM175 (K_{EL}) compared to the bacterial counterparts and suggest events that lead to channel opening. Importantly, our data and conclusions deviate from a previously reported structure and functional investigation [7], in particular regarding the principle of K^+ selectivity.

Results

Crystallization and general architecture of MtTMEM175

From an expression screen of over 30 bacterial TMEM175 channels we identified several homologues as candidates for a structural characterization. However, the crystals for all of the tested homologues, including MtTMEM175, were diffracting maximally to a resolution of 10 Å even in complex with nanobodies (Nbs). Finally, MtTMEM175 was crystallized in complex with a Nb that in turn was engineered by fusing an N-terminally truncated Maltose Binding Protein (MBP) to its C-terminus (Fig. 1a,b and Figure 1–figure supplement 1a,b) which greatly improved diffraction. We solved the structure at a resolution of 2.4 Å using highly redundant data by molecular replacement based on this novel Nb-MBP chaperone, with structures of Nbs and maltose-bound MBP as search models (Supplementary table 1) and could build a map of high quality (Figure 1–figure supplement 2, Figure 1–figure supplement 3 and Figure 1–figure

supplement 4). We named this chaperone scaffold 'macrobody' (Mb) and termed the Mb used in this study Mb_{51H01}. Macrobodies could develop into a promising tool for structural biology applications, especially in electron cryo-microscopy, similar to the recently reported megabodies [13]. Each MtTMEM175 subunit is composed of six transmembrane helices (Fig. 1c) which assemble to form a tetrameric channel as verified using SEC-MALLS of uncomplexed MtTMEM175 (Figure 1–figure supplement 1c). Helix 1 is the pore-lining helix, as predicted earlier [6], and constitutes the highest degree of conservation (Fig. 1c and Figure 1–figure supplement 1d).

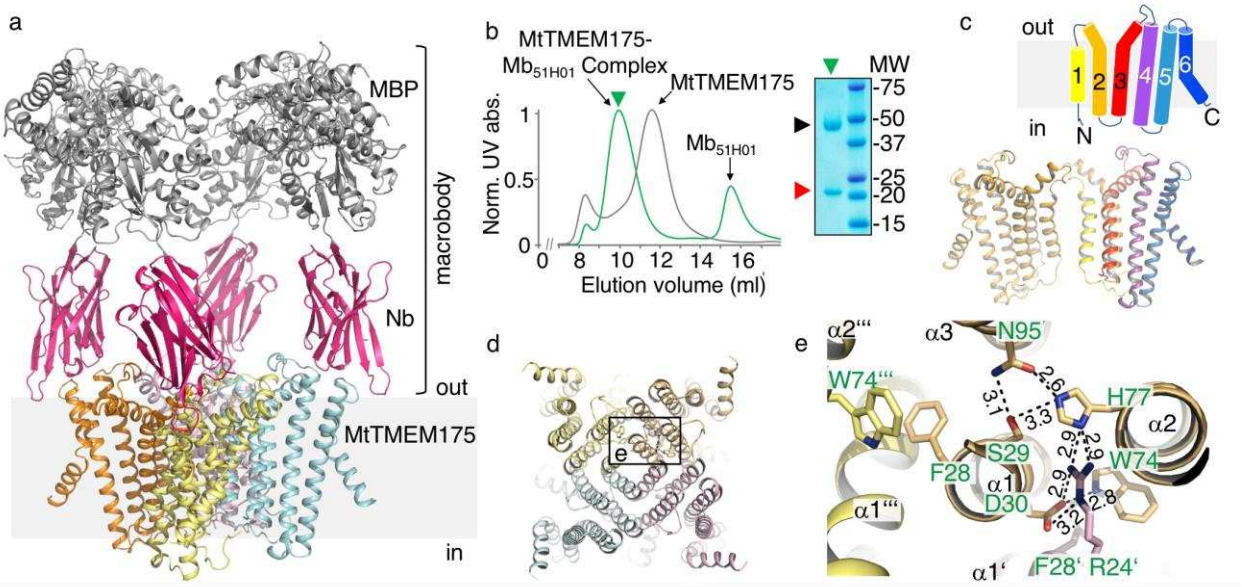

Fig. 1 | Structure of the MtTMEM175-Mb_{51H01} complex
a, Side view of the complex with MtTMEM175 channel and macrobody. Approximate membrane boundaries are indicated. **b,** Left: Size exclusion chromatogram of MtTMEM175 (grey) and MtTMEM175-Mb_{51H01} complex (green). Right: Coomassie-stained SDS-PAGE gel of the peak fraction (▼) indicating complex formation of MtTMEM175 (▼) with Mb_{51H01} (▼). **c,** Arrangement of transmembrane helices 1-6 in MtTMEM175. N- and C-termini are indicated. Two subunits are omitted for clarity. **d,e,** MtTMEM175 tetramer (d) and close-up view on interacting residues with corresponding numbering (e). Distances are given in Å. The view is from the intracellular side.

The MtTMEM175 structure reveals a network of hydrogen bonds in proximity to the intracellular pore entrance that positions helices 1-3 relative to each other and interconnects adjacent subunits (Fig. 1d,e). The network is similar to the one of a recently reported structure of a TMEM175 homologue (CmTMEM175, PDB accession 5VRE) [7] (Figure 1–figure supplement

1e,f) and involves most of the highly conserved residues in TMEM175 channels, also the FSD motif (Phe28, Ser29, Asp30 in MtTMEM175), three consecutive amino acids at the N-terminus of helix 1 that were originally proposed to play a role in ion conduction (Figure 1–figure supplement 1d) [6]. Generally, the level of conservation for TMEM175 channels is strikingly low in transmembrane helices 4-6, persuading us to exclude this region largely from our analysis. The interactions of Ser29, His77 and Asn95 are present in both structures and position the first three transmembrane helices relative to each other. Trp74 from helix 2 is interacting with Asp30 in helix 1 of the same subunit in MtTMEM175, whereas in CmTMEM175 this tryptophan is more involved in a cation-π stack with the phenylalanine from the FSD motif of the adjacent subunit (Fig. 1e and Figure 1–figure supplement 1e,f). Different from CmTMEM175, Arg24 (another highly conserved residue in TMEM175 channels) is interacting with His77 and Asp30 of the adjacent subunit, thereby connecting neighboring subunits (Figure 1–figure supplement 1g). Gel filtration profiles of Arg24 mutant proteins support a role in tetramer assembly (Figure 1–figure supplement 1h). We can thus assign at least one role for most of the highly conserved residues in MtTMEM175, which makes us confident that MtTMEM175 provides a clear case to characterize the TMEM175 family in general. Importantly, the conservation of these key residues in human TMEM175 suggests an overall very similar architecture. None of the aforementioned residues seems to play a distinct role in selectivity that would be immediately apparent from the structure.

MtTMEM175 is a weakly selective K^+ channel

For electrophysiological characterization MtTMEM175 was expressed in HEK293 cells as previously done with homologues from *Streptomyces collinus* and *Chryseobacterium sp.* (ScTMEM175 and CbTMEM175) [6]. In whole cell patch clamp experiments we recorded only from transfected cells non-rectifying, non-inactivating K^+ currents that showed no signs of voltage-dependence (Fig. 2a). These currents were blocked by Zn^{2+} ions and at the applied concentration of 5 mM also in a voltage-independent manner (Fig. 2b). Similar to ScTMEM175 and CbTMEM175, MtTMEM175 has also a low selectivity for K^+ (P_K/P_{Na} ~ 4.3). It conducts Cs^+ and Rb^+ with a similar efficiency as K^+, and to lesser extent, similar to Na^+, also Li^+ (Fig. 2c and Figure 2–figure supplement 1). The channel has no apparent permeability for anions; the reversal voltage was not significantly different when the same recordings were done with standard bath

solution containing the large anion methanesulfonate (+0.64± 3 mV n=18) or in a bath with 150 mM KCl (2.4±4, n=7). We obtained a few single channel recordings from MtTMEM175-transfected cells that revealed a unit conductance of ~70 pS and showed channel flickering (Fig. 2d). We do not have definitive proof that these currents originate from MtTMEM175, however several arguments support this view. First, we recorded them only in transfected cells, which exhibited typical MtTMEM175 macroscopic currents after breaking into the whole cell configuration. Second, like the macroscopic MtTMEM175 current also the single channel I/V relation reverses around 0 mV (Fig. 2d). Finally, the unitary conductance of the channels at -100mV is in the range of the conductance of mock transfected HEK293 cells in whole cell mode (Fig. 2a), making it unlikely that the currents originate from endogenous channels. The presence of gating events is inconsistent with the definition of a leak channel and has significance for the interpretation of the structure.

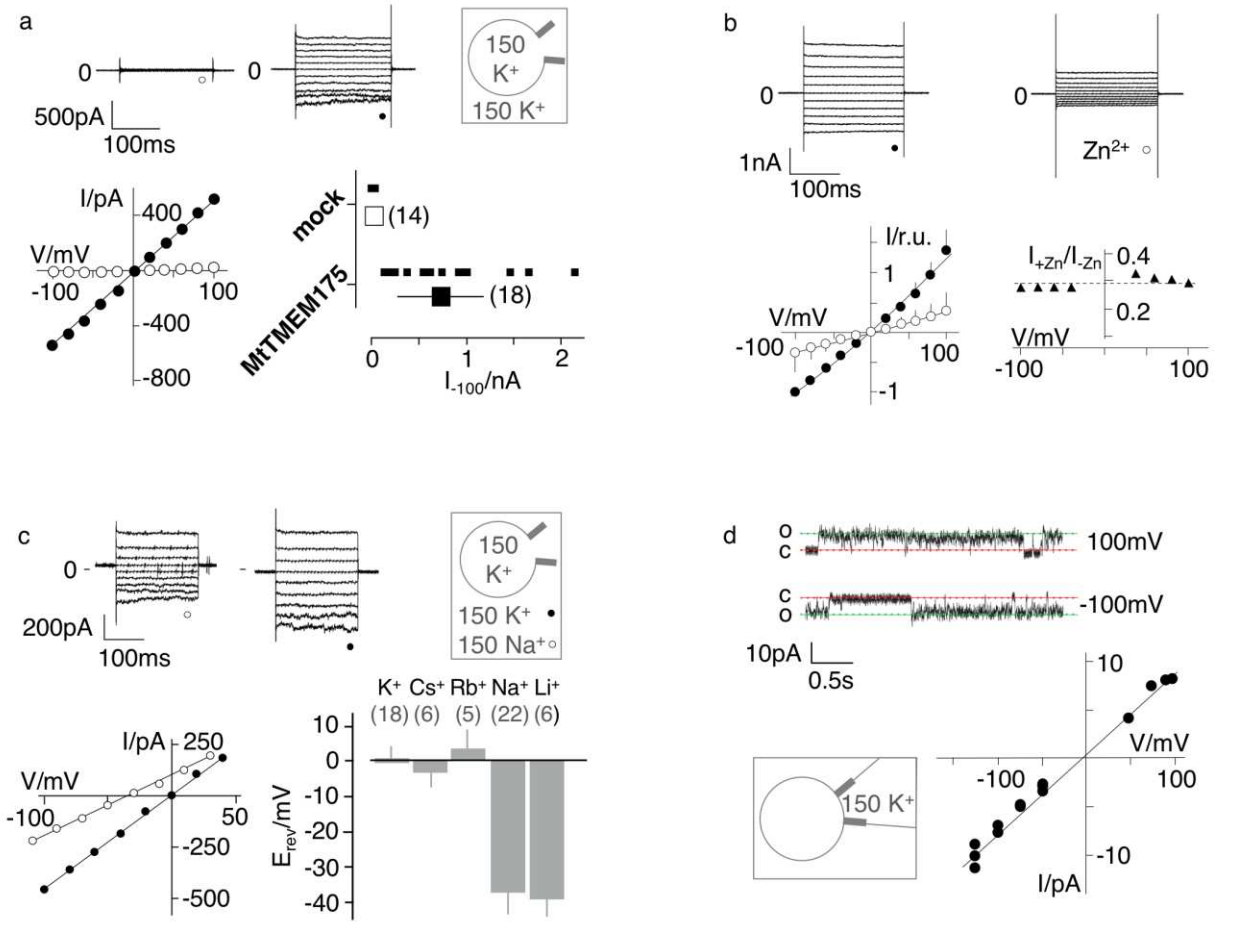

Fig. 2 | Electrophysiological characterization of MtTMEM175

a, Current responses to standard voltage pulse protocol in mock (○) and MtTMEM175 (●) transfected HEK293 cells (upper panel) and corresponding steady state I/V relations (lower left). Plot of currents recorded in same manner at -100 mV for individual cells (small symbols) and mean ± s.d. (large symbols) (lower right). Number of cells in brackets. **b,** HEK293 cells expressing MtTMEM175 before (●) and after (○) adding 5 mM $ZnSO_4$ to the bath solution containing 150 mM K^+ (upper panel). Mean I/V relation (bottom left) of n=4 cells (± s.d.). To compare the effect on different cells the I/V relation was normalized to currents at -100 mV in the absence of blocker (bottom left). The voltage dependency of the Zn^{2+} block was estimated by dividing currents in the presence and absence of Zn^{2+} (I+Zn/I-Zn) (bottom right) **c,** HEK293 cells expressing MtTMEM175 (top row) before (left) and after (middle) replacing Na^+ (○) with K^+ (●) in the external buffer and corresponding I/V relation (bottom left). Same experiments were performed by exchanging K^+ in external buffer by other cations. The mean reversal voltage (E_{rev}) (± s.d., number of cells in brackets) is depicted in lower right panel. **d,** Exemplary channel fluctuations at ±100 mV measured in cell-attached configuration on HEK293 cells expressing MtTMEM175 (upper) and pooled unitary I/V relation of single channel events from 10 measurements in 4 different cells (lower right) using standard bath and pipette solutions.

Albeit currents have been recorded of HEK cells transfected with CbTMEM175, ScTMEM175 and MtTMEM175 ([6] and this study) functional expression of these bacterial channels at the plasma membrane has not been confirmed by other methods. Overexpressed MtTMEM175 with a C-terminal Venus-YFP (vYFP) indicated a wide distribution, without a prominent presence at the plasma membrane (Figure 2–figure supplement 2a). Thus, we generated plasma membrane patches by decapitation of cells with ice cold distilled water [14]. In the membrane from transfected and control cells we could show with TIRF microscopy that vYFP-tagged MtTMEM175 and hTMEM175 also co-localize with specific plasma membrane stains in HEK293 cells (Figure 2–figure supplement 2b). In a second experiment we purified C-terminally vYFP-tagged Nb_{51H01} (Nb_{51H01}-vYFP) from transiently transfected HEK cells (Figure 2–figure supplement 3a) and incubated unfixed HEK cells that were mock-transfected or transfected with non-fluorescent MtTMEM175 with the purified fluorescent Nb_{51H01}-vYFP. Nb_{51H01} recognizes an extracellular epitope of MtTMEM175 (Fig.1a) and is thus suitable to label non-permeabilized cells that expose MtTMEM175 on the plasma membrane. Figure 2–figure supplement 3 clearly shows that Nb_{51H01}-vYFP is only labeling HEK cells transfected with MtTMEM175 and provides evidence for at least partial plasma membrane localization and correctly folded MtTMEM175 channels. Further, non-fluorescent MtTMEM175 purified from transiently transfected HEK cells elutes as a tetramer in SEC at near identical volumes as bacterially expressed MtTMEM175 (Figure 2–figure supplement 4). Together, these results are in support of functional plasma membrane expression of MtTMEM175 in HEK cells and in concordance with our electrophysiology data.

The MtTMEM175 structure reveals hydrated and dehydrated K^+ ions

The structure of MtTMEM175 revealed two densities attributable to K^+ ions, termed $1K^+$ and $2K^+$ (Fig. 3a-c). The presence of K^+ is supported by data collection at higher wavelengths of 2.02460 Å (Figure 3–figure supplement 1a,b and Supplementary table 1). In contrast, the structure of CmTMEM175, which was solved at 3.3 Å did not reveal bound ions, even in crystals soaked with heavier monovalent and divalent ions [7]. One K^+ ion ($1K^+$, occupancy ~1) in the MtTMEM175 structure, is located at an ion binding site at the extracellular pore entrance (Fig. 3b). This binding site resembles a short selectivity filter [15-17]. The K^+ ion is complexed by eight water molecules in an anti-prismatic geometry (Figure 3–figure supplement 1c) that are coordinated by backbone oxygens of Leu42, Ser43 and Ser44 (Fig. 3b,d and Figure 3–figure supplement 1d). The respective backbone oxygens of these residues are 12, 13.1 and 14.9 Å apart (Fig. 3d). Except for the conserved Leu42, no obvious motif for this region is apparent (Figure 1–figure supplement 1d).

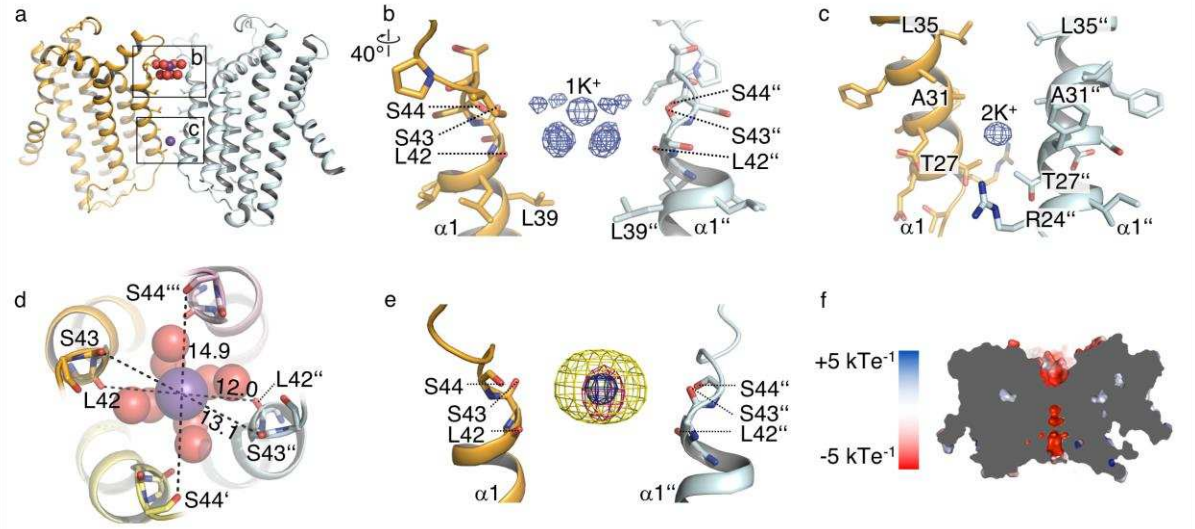

Fig. 3 | Ions in the MtTMEM175 structure

a-c, Side view on MtTMEM175 (a) and close-up views of the ion binding site with a hydrated K^+ ion at position $1K^+$ (b) and another K^+ ion within the pore at position $2K^+$(c). In (a), K^+ ions and water molecules are displayed as purple and red spheres, respectively. In (b) and (c) the $2F_o$-F_c electron density is depicted as blue mesh at the position $1K^+$ and $2K^+$ (at 2.4 Å, contoured at 1.8 σ, sharpened with b=-25). Two subunits are omitted for clarity. **d,** Top view of the ion binding site. Distances between opposing backbone oxygens of Leu42, Ser43 and Ser44 are indicated in Å. Side chains are omitted and the size of the spheres is reduced for clarity. **e,** Substitution of K^+ in the ion binding site with Cs^+ and Rb^+. The $2F_o$-

F_c electron density (as in (b) and (c), blue mesh) marks the position of the K^+ ion. Anomalous difference electron densities of Cs^+ (at 3.8 Å, contoured at 7 σ) and Rb^+ (at 3.6 Å, contoured at 7 σ, blurred with b=125) are shown in yellow and magenta, respectively. **f,** Illustration of the surface electrostatic potential across the pore.

The second K^+ ion ($2K^+$, occupancy ~0.5) is not coordinated by water molecules which suggests the permeation of dehydrated K^+ ions in these channels. The K^+ ion at position $2K^+$ is located between the layers of Leu35 and Thr27 (Fig. 3a, c). It is likely that this K^+ ion is trapped in the pore due to the restriction at Thr27 and the lack of clear interactions with the protein. It is further worth to note that the density at 2 K^+ is likely also partly constituted by Na^+ ions. The anomalous signal (Figure 3–figure supplement 1a,b) at this position is proportionally weaker in comparison to the signal at $1K^+$ than in the native data set (Fig. 3b,c). We can therefore only estimate that the occupancy at $2K^+$ is approximately ~0.5. By soaking crystals with Cs^+ and Rb^+ we detected clear anomalous density for both ions at the position of $1K^+$ (Fig. 3e) providing additional evidence for an affinity towards monovalent cations with similar properties as K^+ at this extracellular ion-binding site. No significant anomalous signal for Cs^+ or Rb^+ was found at the $2K^+$ position, indicating that the channel would have to open for diffusion of these generally permeable ions to this position. Collectively, these results advocate the existence of a conductive conformation with a wider pore that is different from the crystal structure. Additional density in the $2F_o$-F_c map on the extracellular side in proximity to the ion binding-site was attributed to a maltose moiety from a detergent molecule. We tested for potential influence of maltose on the conductance by electrophysiology, but could not detect any effects (Figure 2–figure supplement 1).

The hydrated K^+ ion in the MtTMEM175 crystal is reminiscent of the one in the vestibule of a high-resolution structure of KcsA in close proximity to the selectivity filter entrance [18]. In comparison, the two planes in the K^+-hydrate in MtTMEM175 are skewed, due to interactions with the surrounding backbone oxygens (Figure 3–figure supplement 1c-e). The eightfold coordination of K^+ ions in square antiprism is also seen inside the canonical selectivity filter, where it is mediated by backbone oxygens (Figure 3–figure supplement 1e) [12,18]. MtTMEM175 crystallized in the presence of equimolar amounts of Na^+ and K^+ which apparently did not interfere with K^+ coordination at $1K^+$. The ion binding site thus recapitulates a number of central elements seen in K^+ coordination of ion channels, in particular the coordination geometry. However, the low conservation, its simplicity, the indirect coupling of the K^+ ion to the backbone

oxygens and the single binding site make it questionable that this region determines selectivity. It could be that this binding site serves to attract monovalent ions with similar properties as K^+ and plays a role in the resolvation or desolvation of K^+ ions that pass through the pore. Apart from the ion binding site, the negative electrostatic potential in the pore lumen would be another property promoting cation permeation (Fig. 3f).

Bulky residues constrict the pore and form a physical gate in the closed state

In the structure of MtTMEM175 Leu35 is occluding the pore to such an extent that K^+ ions could not pass (Fig. 4). This bulky residue is thus likely constituting a hydrophobic physical gate. From single channel recordings and the lack of exchangeability of $2K^+$ with Cs^+ or Rb^+ we have indications for open and closed conformations in support of a gate in TMEM175 channels. Due to the highly constricted pore, the structure of MtTMEM175 thus very likely represents a closed state and this implies that structural rearrangements have to take place in order for the channel to become conductive. Opening of the channel would inevitably require displacement of the hydrophobic side chain of Leu35 from the pore center, probably by a helix-rotation as seen in the NaK channel [19] or in TRPV6 [20]. Previously, the homologous residues in CmTMEM175 (Ile23) or human TMEM175 (Ile46 and Ile271) were described as the determinants for selectivity [7], however we propose that this position is generally occupied by a residue that acts as a physical gate for ions as discussed below in more detail. Furthermore, the pore-lining residues that physically interact with passing ions and determine conduction or selectivity would likely show the highest degree of conservation.

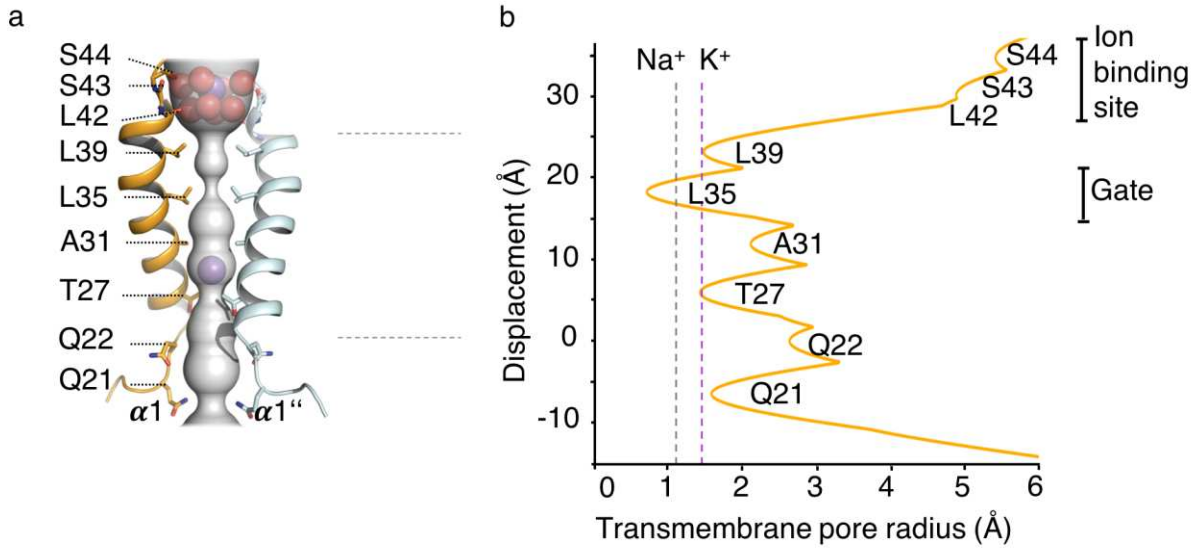

Fig. 4 | HOLE analysis

a, The ion conduction pathway is illustrated as grey surface and pore-lining residues are displayed. K^+ ions and water molecules are shown as purple and red spheres, respectively. **b,** The pore radius along the central axis is shown in Å. Dashed lines indicate the radii of K^+ and Na^+ ions without inner hydration shell.

When we plotted the conservation of residues from an AL2CO analysis of randomly chosen TMEM175 proteins onto the structure of MtTMEM175 (see Methods section) we found that the most highly conserved residues are not the bulky hydrophobic residues that face the pore in the observed conformation. The more conserved residues are located to the side of the pore-lining helix, facing helix 1 of the next subunit (Figure 4-figure supplement 1). In MtTMEM175, these are the residues Thr38, Ala34 and Asp30 (the latter being part of the FSD motif and involved in hydrogen bonds to Arg24 and Trp74). Threonine38 and Ala34 do not show any particular interaction with their respective environments, e.g. with the adjacent helix that they are facing, raising the question why these residues have such a high degree of conservation. In particular Thr38 is of interest since it is the most conserved residue among all TMEM175 proteins (Figure 4-figure supplement 1e and Fig. 5a, c). Threonine38 forms a layer that is interspersed between Leu35 and Leu39 and participates in a bifurcated hydrogen bond with the main-chain oxygen of Ala34 (Figure 5-figure supplement 1a,b). A rotation of helix 1 (in clockwise direction when viewed from intracellular) as part of an iris-like opening of the gate (Leu35), would expose the side chain of Thr38 to the pore lumen. Following this line of thoughts, we reasoned that K^+ ions

297 could interact with the side chain of Thr38 in a conductive conformation of MtTMEM175 and
298 mutated Thr38 to alanine.

299 ## The highly conserved Thr38 confers K^+ selectivity to the MtTMEM175 channel

300 When analyzed in whole cell patch clamp recordings in HEK293 cells the T38A mutant of
301 MtTMEM175 showed a strongly impaired selectivity for K^+ ions, as exchanging K^+ in the bath
302 solution for Na^+ caused only a minor shift of the reversal potential by –15±2 mV (n=4),
303 corresponding to a $P_K/P_{Na}<2$ (Fig. 5b). For comparison, the WT protein responds to a
304 replacement of K^+ for Na^+ with a shift of –37±6 mV (n=22) (Fig. 2c and Fig. 5b). When we
305 mutated Leu35 to alanine the channel showed only a slightly reduced selectivity compared to
306 WT channels (E_{rev}= -31±2 mV, n=6) (Fig. 5b), in contrast to the findings on Ile23 for
307 CmTMEM175 and Ile46/Ile271 in hTMEM175 [7]. Our data speaks against a primary function in
308 selectivity for these bulky hydrophobic residues as discussed below. We thus conclude that
309 Thr38 plays a pivotal role for K^+ selectivity and conductance in MtTMEM175, reflected also in
310 its high degree of conservation (Figure 4-figure supplement 1e). Notably, the side chain of a
311 conserved threonine is also essential for the coordination of K^+ ions at the S4 position in the
312 selectivity filter of canonical K^+ channels. Hence, not only carbonyl ligands, but also the
313 threonine side chain is suited to coordinate K^+ ions with impact on selectivity and conductance
314 [21-24]. We found no obvious differences in a crystal structure of this mutant in the closed
315 conformation (Figure 5-figure supplement 1c,d and Supplementary Table 2). Overall, a
316 significant contribution to K^+ selectivity by the extracellular ion binding site is contradicted by
317 the results for the T38A mutant protein - whether the residual selectivity is arising from this
318 motif remains open. Ascribing a function to the extracellular ion binding site is thus currently
319 difficult. Structural insight into the conductive conformation, which might reveal rearrangements
320 at both ends of helix 1, will help to gain insight into potential functions of this region. The
321 binding site could also serve an unrelated function, e.g. sensing of ions to modulate the open-
322 probability.

323 ## A layer of threonines also accounts for K^+ selectivity in human TMEM175 channels

324 The layer of threonines is also conserved in vertebrate TMEM175 proteins (Fig. 5c) and we thus
325 tested if mutating the corresponding residues to alanine in the human TMEM175 channel would
326 affect selectivity. Human TMEM175 is more selective than the bacterial counterparts with

reported values of P_{Cs}/P_{Na} of approximately 20 [6,7]. We measured currents from cells expressing hTMEM175 at the plasma membrane as previously done [7]. From the shift in the reversal voltage after replacing K^+ for Na^+ in the external medium (-58 ±3, n=7) we estimate a P_K/P_{Na} value of ~10 (Fig. 5d), lower than the reported P_{Cs}/P_{Na} values of hTMEM175. This discrepancy is likely due to the fact that we used K^+ as internal cation and not the 1.5-fold more permeable Cs^+ [6,7]. Mutating Thr49 in the first repeat and Thr274 in the second repeat of hTMEM175 to alanine resulted in strongly reduced selectivity with a reversal potential of -17±3 (n=8) when exchanging K^+ for Na^+ in the external solution (Fig. 5d), providing evidence for a conserved role of the threonine-layer in selectivity. Since the human channel is 2-3 times more selective as the known bacterial counterparts there must thus be an additional factor that accounts for the increased selectivity, probably in conjunction with the threonine layer.

Serine45 increases K^+ selectivity in human TMEM175

When comparing the primary sequences of vertebrate genes, we found that the position that is corresponding to the highly conserved Ala34 in MtTMEM175 is occupied by serine in repeat 1 for all of the analyzed vertebrate species (Ser45 in hTMEM175), while in repeat 2, like in bacterial channels, the corresponding residue is an alanine (Ala270 in hTMEM175) (Fig. 5c and Figure 5–figure supplement 1e,f). We have thus suspected that Ser45 might also play a role for selectivity in hTMEM175 in an analogous manner as the threonines. The side chain of these serines could contribute to coordination of K^+ ions in close proximity to the threonine layer to increase selectivity, i.e. six ligands would be involved in ion coordination instead of only four as in MtTMEM175. In the S45A mutant dimer, selectivity was indeed reduced with a reversal potential of -27±2 (n=24) upon changing the major cation in the bath solution from K^+ to Na^+. This mutant is very similar to bacterial TMEM175 channels in its primary sequence of helix 1 and intriguingly also with respect to its preference for K^+. Consequently, a triple mutant where all of the threonine and serine residues in these two layers of the pore are exchanged for alanine (S45A/T49A/T274A) shows a similar reduction of selectivity (E_{rev}= -22±3 mV, n=8) (Fig. 5d) as the double mutant T49A/T249A and the T38A mutant protein of MtTMEM175 (Fig. 5b). We thus conclude that Ser45 in the first repeat is accounting for the increased selectivity of the human TMEM175 channel, but in conjunction with the threonine layer.

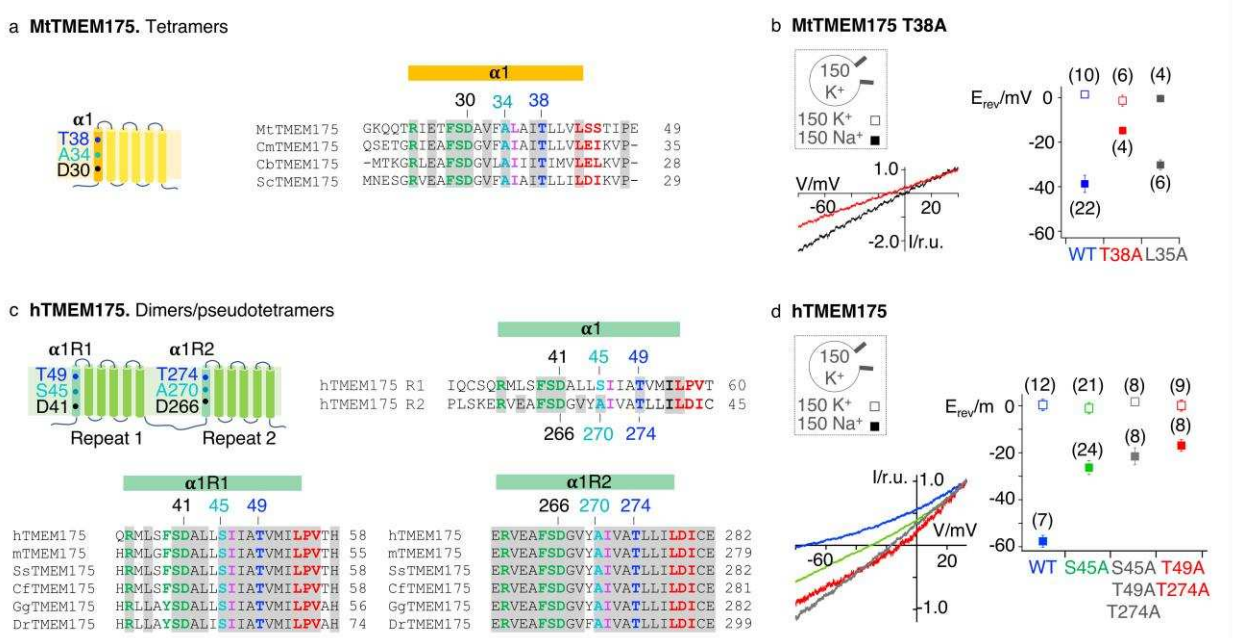

Fig. 5 | K^+ selectivity in TMEM175 proteins

a, Subunit organization of MtTMEM175 and alignment of bacterial sequences highlighting the most conserved residues in helix 1. **b,** Lower left: representative currents elicited by a ramp protocol (-80 to +40 mV in 200 ms) from HEK293 cells transfected with the MtTMEM175 T38A in external solution with 150 mM K^+ (black) or Na^+ (red); currents normalized to values at +33 mV. Right: plot of the average reversal potentials (E_{rev} ± s.d.) for T38A or L35A mutants in comparison to WT in symmetrical buffer with 150 mM K^+ (□) or in external buffer with 150 mM Na^+ (■). Number of patched cells in brackets. **c,** Subunit organization of hTMEM175 and alignment highlighting conserved residues. m: mouse, Ss: *Sus scrofa*, Cf: *Canis familiaris*, Gg: *Gallus gallus*, Dr: *Danio rerio* **d,** Lower left: representative currents elicited by a ramp protocol as in (a) from HEK293 cells transfected with hTMEM175 WT (blue) or mutants S45A (green), T49A/T274A (red) or S45A/T49A/T274A (grey) in external solution with 150 mM Na^+; currents normalized to values at +33 mV. Right: plot of the respective average reversal potentials (E_{rev} ± s.d.) for each construct in symmetrical buffer with 150 mM K^+ (□) or in external buffer with 150 mM Na^+ (■). Number of patched cells in brackets.

As the total number and geometry of the coordinating ligands accounts for selectivity, it is clear that mutation of the threonine layer suffices to lose selectivity since the remaining two serine residues alone could not effectively coordinate K^+ ions. Generally, reduction of sequential ion binding sites is known to attenuate the K^+ selectivity in the canonical K^+ selectivity filter, whereas introducing additional binding sites can increase selectivity [25-30], a principle that apparently also accounts for the different K^+ selectivity of bacterial and vertebrate TMEM175 channels.

Zinc ions and 4-aminopyridine act as pore blockers at the selectivity filter of hTMEM175

Next, we sought to gain insight into the mechanism of channel blocking in TMEM175 proteins. In comparison to bacterial TMEM175 channels, the human TMEM175 channel is substantially more sensitive to Zn^{2+} ions (IC50 ~ 38 µM compared to an estimated IC50 of ~0.5 mM for bacterial homologues [6]). In addition, the human channel is also inhibited by the potassium-channel blocker 4-AP (IC50 ~35 µM) [6], indicating significant differences between human and bacterial homologues and suggesting a more specific interaction of the blockers with the human channel. The equally effective block of human TMEM175 by Zn^{2+} and 4-AP regardless of extracellular or intracellular application [6,7] is a good indication that the block is occurring in the pore. We have shown that the increased selectivity for K^+ in hTMEM175 is founded on Ser45, and thus assumed that the pronounced sensitivity for Zn^{2+} and the potency of 4-AP could also be based on this difference. To address this question, we analyzed the response of the S45A mutant of hTMEM175 for these blockers in comparison with the WT protein. As shown in Fig. 6a and b, the S45A mutant is not blocked by Zn^{2+} ions and also lost its sensitivity for 4-AP at a concentration of 100 µM.

These data confirm that both Zn^{2+} and 4-AP act as pore blockers at the selectivity filter, at very similar locations. The size of the 4-AP molecule further suggests that this block can only take place in a widened pore which again implies a different conductive conformation where bulky side chains do not occlude the ion path and Ser45 is facing the pore.

Bacterial channels are only weakly inhibited by Zn^{2+} [6] and the S45A mutant of hTMEM175 suggests that the threonine layer constituted of Thr38 in MtTMEM175 and Thr49/Thr274 in hTMEM175 does not suffice to render TMEM175 channels sensitive to Zn^{2+}. Indeed, the T38A mutant of MtTMEM175 retained its sensitivity for Zn^{2+}; in WT and the mutant channel Zn^{2+} caused at a reference voltage of -60 mV the same relative inhibition (WT 66.9±12%, T38A mutant 69.7 ±10 n= 4) (Figure 6–figure supplement 1a). This suggests that the bacterial channel is inhibited by Zn^{2+} through a different mechanism, i.e. not a pore block. In seeming contrast to this finding we could clearly localize anomalous signal of Zn^{2+} ions in the pore by soaking crystals of MtTMEM175 with 0.5 mM Zn^{2+}. The major peak of this anomalous signal (when contoured at 4σ) lies in proximity to Thr38 and Leu35 (Figure 6–figure supplement 1b). In crystal soaking experiments with the T38A mutant of MtTMEM175 we could not detect anomalous signal for Zn, even when using concentrations of 2.5 mM (0.5-2.5mM tested) and contouring of the anomalous signal at 4σ and 2σ (Figure 6–figure supplement 1c). This supports

an attraction for Zn^{2+} ions in the pore in close distance to, or directly at the selectivity filter and indicates that the T38A mutation changes the electrostatic environment in the pore. However, our functional analysis does not support the idea that Zn^{2+} is blocking MtTMEM175 by the same mechanism as hTMEM175.

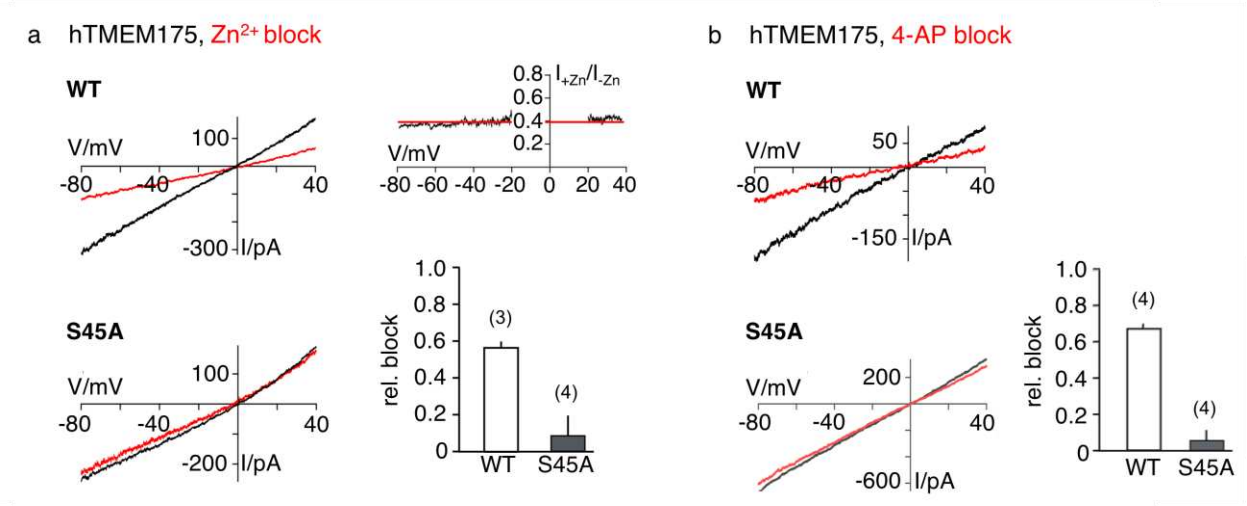

Fig. 6 | Sensitivity of the hTMEM175 S45A mutant for Zn^{2+} and 4-AP

a, Currents elicited by a ramp protocol (-80 to +40 mV in 200 ms) in HEK293 cells expressing hTMEM175 WT (upper left) or hTMEM175 S45A mutant (lower left) in absence (black) and presence (red) of 5 mM $ZnSO_4$ in external bath solution (150 mM K^+). Columns (lower right) summarize average inhibition (± s.d.) of current amplitudes at -60 mV from 3 and 4 recordings in the hTMEM175 WT and S45A mutant, respectively. The ratio of currents in the presence and absence of Zn^{2+} (I+Zn/I-Zn) show the voltage independence of channel block (upper right). **b**, same as in (c) with representative measurements in absence (black) or presence (red) of 100 µM 4-AP in external bath solution (150 mM K^+) for hTMEM175 WT (upper left) and S45A mutant (lower left), respectively. Columns show average inhibition (± s.d.) of current amplitudes at -60 mV from 4 measurements in the hTMEM175 S45A mutant and WT, respectively.

Discussion

The TMEM175 family of non-canonical potassium channels has recently been identified to confer a K^+ selective conductance to lysosomes and late endosomes [6]. Importantly, it has been shown that this channel is presumably involved in the early onset of PD [8-10,31]. Even though its exact function in lysosomal physiology still needs to be clarified the available experimental evidence shows that aberrant processing of autophagosomes as well as an increased lysosomal pH under conditions of starvation is the prominent phenotype of TMEM175-loss [6,8] and likely connects this lysosomal pathology to PD. In combination with an electrophysiological analysis

the high-resolution MtTMEM175 structure provides a solid framework on which we identify the residues that confer K^+ selectivity in this channel family.

Selectivity in TMEM175 channels

From the structural analysis we divide the pore of TMEM175 channels into functional layers (Fig. 7a), conceptually different from a previous interpretation [7]: The TMEM175 ion pathway is built from an ion binding site for monovalent cations (with properties similar to K^+ ions) at the extracellular pore entrance, a major gate at the position of Leu35 (MtTMEM175) and, rather unusual, by one (in prokaryotes) or two interspersed polar layers (in vertebrates) that tune K^+ selectivity. Our observations and conclusions are based on two important considerations. First, scrutiny of the pore in the structure of MtTMEM175 shows that it is too narrow for the passage of ions. This demands that conformational changes have to take place in order to make the channel conductive. Second, there are highly conserved hydrophilic side chains (from threonine and additionally serine in vertebrate counterparts) that would be suited for coordinating ions on their passage. But since these residues do not face the pore lumen we anticipate a rotation of helix 1, resulting in an iris-like opening in assembled TMEM175 channels as a plausible route for transitioning into a conductive conformation. Such a rotation simultaneously exposes the hydroxyl-groups of the threonines (Thr38 in MtTMEM175 and Thr49/Thr274 in hTMEM175) and serines (Ser45 in hTMEM175) to the pore lumen and swings the bulky hydrophobic residues (Leu35 in MtTMEM175) out of the conducting pathway (Fig. 7b). Indeed, mutating the respective threonine and serine residues strongly reduced the cation selectivity both in bacterial and vertebrate TMEM175 channels (Fig. 5b,d).

Intriguingly, in hTMEM175 the selectivity could be attenuated to levels of bacterial homologues by reducing the number of coordinating ligands from six to four through mutation of Ser45 to alanine. How exactly the presence of these two additional hydrophilic residues leads to a preference for K^+ over Na^+ ions remains to be seen. But as previously mentioned, a higher number of coordinating ligands seems to be a general mechanism for achieving a high K^+ selectivity also in other K^+ channels [25-30].

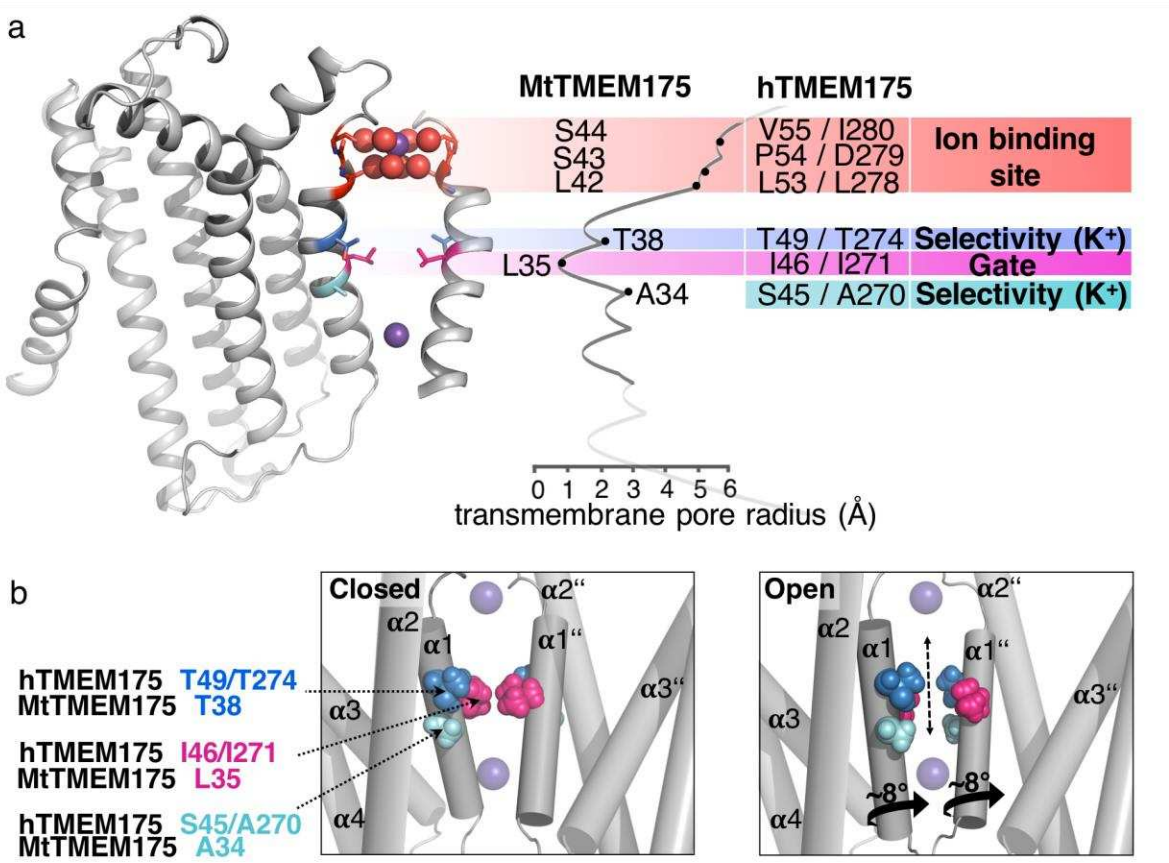

Fig. 7 | Functional layers and proposed mechanism for channel opening in TMEM175 channels
a, Functional layers in the MtTMEM175 pore. Two subunits are shown (right side only partly). Important residues in MtTMEM175 and hTMEM175 and for comparison the pore radius (in Å) are indicated. The ion binding site is shown in red, gate-residues in magenta and residues required for selectivity in blue and cyan. **b,** Schematic side view of MtTMEM175 in closed (left) and proposed conductive state (right). Key residues on helix 1 are shown as spheres. Two subunits are omitted for clarity. K^+ ions are shown as purple spheres. A clockwise rotation of helix 1 (viewed from intracellular) of 8-15° would widen the pore sufficiently for K^+ ions to permeate (indicated by curved arrows in the bottom panel).

The proposed mechanism for K^+ selectivity in TMEM175 channels is also backed by our finding that Ser45 is underlying a pore block by Zn^{2+} and 4-AP in hTMEM175 at the site of the selectivity filter, underscoring that the respective Ser residues are part of the conductive pathway. The data further suggests why bacterial channels are less sensitive or resistant to these agents with only four ligands in their simpler selectivity filter.

Another unusual finding is the voltage independence of the pore block in hTMEM175 (Fig. 6a), as this is expected for a binding site in the electric field of the channel [32]. How can this be explained? We can currently only speculate but one reason could be that TMEM175 channels spontaneously open and close without a trigger, different from voltage- or ligand-gated ion

channels. When they are open, the binding site for the pore blocker is accessible and the blocker could bind. It is worth to note that in our crystal soaks the small Zn^{2+} ion was found even in the closed channel nearby the selectivity filter in the middle of the membrane plane (Figure 6–figure supplement 1b). This means that the Zn^{2+} ion (or the 4-AP molecule) is already bound at the selectivity filter before a voltage is applied for eliciting a current. In such a scenario voltage may not affect the strength of the block.

In summary, our data advocate a model which provides a coherent description of selectivity, blocking and channel opening. However, definite conclusions have to await additional evidence from an open channel structure.

Structural differences between MtTMEM175 and CmTMEM175

Comparison of the previously reported structure of CmTMEM175 [7], with the model of MtTMEM175 highlights a number of significant differences, which potentially bear information on the function of TMEM175 type channels.

One crucial difference is located at the cytosolic entrance to the pore and could be related to a pH dependent gating mechanism. While both structures reveal a hydrogen-bond network on the intracellular side within helices 1-3, only the MtTMEM175 structure exhibits an additional interaction between His77 with Arg24, which connects two adjacent subunits. The corresponding arginine in CmTMEM175 is in contrast not clearly resolved (Figure 1–figure supplement 1g). Since MtTMEM175 was crystallized at a pH of 8.5 and CmTMEM175 at a pH of 4.5 it is most likely that His73 in CmTMEM175 (corresponding to His77 in MtTMEM175) is protonated and hence repulsing the arginine. A transient pH-sensitive disengagement of this arginine from the histidine (and Asp30) could be a step in the opening of the channel. This would be achieved by loosening interactions of the N-terminal end of helix 1 with the adjacent subunit as already indicated in the CmTMEM175 structure which shows a more open pore at the intracellular side compared to MtTMEM175 (Figure 6–figure supplement 2c).

Another difference between the structures is apparent at the extracellular tip of helix 1 where both structures are substantially deviating. This can explain the lack of coordinated ions in the CmTMEM175 structure (Figure 3-figure supplement 1i,k). Notably, only the extracellular end of helix 1 in the CmTMEM175 structure contains a 3_{10}-helix over a stretch of 3-4 residues and thus extends further than helix 1 in MtTMEM175 (Figure 3-figure supplement 1f,g). As a

consequence the backbone oxygens are too distant from the pore axis for interacting, like in the MtTMEM175 structure, with the water molecules of a K^+-hydrate (Fig. 3a,b,d and Figure 3-figure supplement 1i,k). 3_{10}-helices are commonly associated with transition states and thus hint to dynamic regions within a helix [33]. Whether the CmTMEM175 structure represents such an intermediate conformation (albeit likely not a true transition state) remains to be investigated.

It is furthermore worth noting, that the short helix between the helices 1 and 2 of CmTMEM175 is involved in major crystal contacts, which might be responsible for a displacement of the tips of helix1 and formation of the 3_{10}-helix (Figure 3-figure supplement 1h). Even though our results indicate that the coordinated K^+ ion has no direct impact on the selectivity of the MtTMEM175 channel, this configuration may still be relevant for function. However, the 3_{10}-helix in CmTMEM175 has also an influence on the position of other pore lining side chains when compared to MtTMEM175. This is in particular true for Leu30, which is facing the pore in contrast to the equivalent Leu42 in MtTMEM175 (Figure 6-figure supplement 2a,b). Leucine30, Leu27 and Ile23 in CmTMEM175 are thereby forming three layers of pore-lining hydrophobic residues. This scenario is reminiscent of the structures of bestrophins, e.g. a channel to which CmTMEM175 was primarily compared in literature [7]. It was proposed that Ile23, which is part of the triad of bulky pore lining residues in CmTMEM175, conveys the K^+ selectivity as a hydrophobic selectivity filter, as initially also proposed for bestrophins [34,35]. Mutation of Ile23 or corresponding residues in hTMEM175 to small or hydrophilic residues indeed resulted in a loss of K^+ selectivity [7]. If Ile23 however acts as a gate to keep the channel closed, a role that we suggest for the corresponding Leu35 in MtTMEM175, an exchange for asparagine or alanine would likely result in a permanently open channel (Figure 6-figure supplement 2d). For instance, in bestrophins, mutation of three layers of bulky residues along the ion path to alanine resulted in an open channel, without the requirement for activation [36,37]. This supported a function of these residues as a gate instead of contributing to selectivity. Similarly, mutation of a gate built from phenylalanine in the NaK channel strongly increased flux [19]. More recently a cryo-EM structure of chicken bestrophin in a conductive conformation provided evidence against a role of the bulky pore-occluding residues as hydrophobic selectivity filters but instead revealed that these residues are indeed physical gates [38]. Hence mutation of hydrophobic gates with small and/or hydrophilic residues can have substantial impact on the closure and conduction of ion channels [37,39,40]. When we mutated Leu35 to alanine we could only see small effects on the selectivity, speaking against

a role in selectivity (Fig. 5b). Probably this mutant allows for some non-specific permeation in closed state due to the loss of the leucine-gate which results in slightly reduced selectivity in whole-cell recordings when compared to WT.

Conclusions

TMEM175 channels are not as enigmatic as anticipated earlier but instead recapitulate classical structure-function correlates of other ion channel families: Large hydrophobic residues are acting as gates and polar contacts from side chains and the backbone are coordinating ions in the conducting pathway. On the other hand, it is remarkable that the selectivity is mediated by cryptic hydroxyl-bearing side chains inside the pore that are only available for selective ion solvation in an open conformation by concerted repositioning. In conclusion, the conductive state must thus deviate substantially from the closed state in order to be permeable to ions. This is strongly supported by the localization of the residues that mediate K^+ selectivity and sensitivity to the blockers Zn^{2+} and 4-AP. Collectively this study provides insight into an alternative solution for conduction of K^+ ions and an unusual selectivity filter. But with respect to the geometry, chemistry and the number of ligands the channel architecture also recapitulates established concepts of K^+ channel biophysics.

Data availability: Atomic coordinates have been deposited at the Protein Data Bank with the following unique identifiers: 6HD8, 6HD9, 6HDA, 6HDB, 6HDC, 6SWR.

The following previously published data set was used: PDB entry 5VRE. Lee, C. et al. The lysosomal potassium channel TMEM175 adopts a novel tetrameric architecture. *Nature* **547**, 472-475 (2017).

Acknowledgments: We are grateful to R. Dutzler (University of Zürich) for support, providing materials and lab infrastructure. We thank B. Blattmann and C. Stutz-Ducommun (Crystallization facility at University of Zürich) and the Swiss Light Source (PSI-Villigen) for excellent support. S. Stefanic and P. Deplazes (Nanobody Facility, University of Zürich) are acknowledged for immunization of alpacas. Calculations were performed at sciCORE (http://scicore.unibas.ch/) scientific computing center (University of Basel). We thank B. Dreier (University of Zürich) and T. Sharpe (University of Basel) for help with the MALLS experiment.

We thank members of the Dutzler lab/Zürich and Maier lab/Basel for many fruitful discussions. A.M. and G.T. thank Henry Colecraft (Columbia University) for hospitality in his laboratory. We thank Robert Lehn (TU Darmstadt) for the help with TIRF microscopy. We thank Ronnie Willaert (VUB Brussels) and Charlotte Yvanoff (VUB Brussels) for help with the Nikon Eclipse Ti2 microscope. This work was supported by 2016 Schaefer Research Scholars Program of Columbia University to A.M., and European Research Council (ERC) 2015 Advanced Grant 495 (AdG) n. 695078 noMAGIC to A.M. and G.T..

Competing interests: The authors declare no competing interests.

Figure-figure supplement lengends:

Figure 1–figure supplement 1 | Macrobody, sequence alignment of TMEM175 proteins and tetramer assembly

a, Dimensions of the Mb_{51H01} fusion protein and a Fab (anti-KcsA, 5J9P) in comparison. **b,** Macrobody expression construct. PelB: PelB leader sequence, His_{10}: deca histidine-tag, MBP: maltose binding protein, 3C: 3C protease cleavage site, Nb: nanobody. **c,** Multi angle laser light scattering (MALLS) coupled to a Superdex 200 (10/300) column, injected with MtTMEM175, after removal of tags. The molar mass is indicated: red, MtTMEM175, blue, detergent micelle of DDM, green, MtTMEM175 with

DDM detergent micelle. The calculated molecular weight of the MtTMEM175 tetramer is 116 kDa. Grey line: UV absorption at 280nm, dashed grey line: refractive index, black line: light scattering. **d,** Sequence alignment of the N-terminal part of characterized TMEM175 family members. Mt: *Marivirga tractuosa*, Cm: *Chamaesiphon minutus*, Cb: *Chryseobacterium sp.*, Sc: *Streptomyces collinus*, h: human. For hTMEM175 both repeats (R1, R2) were included in the alignment. Transmembrane helices from the MtTMEM175 structure are indicated by orange bars with corresponding numbering. Identical amino acids are marked in grey. Residues participating in a conserved hydrogen bond network between helices 1-3 are colored in green. Residues of the ion binding site are colored red while residues that confer K^+ selectivity in MtTMEM175 and hTMEM175 are indicated in blue and cyan. Residues that form the gate are shown in magenta. **e,f,** Tetramer assembly in CmTMEM175 (5VRE) (e) and close-up view on interacting residues with corresponding numbering (f). Distances are given in Å. The view is from the intracellular side. **g,** Interactions of the conserved arginine in helix 1 in MtTMEM175 and CmTMEM175. The view is from the intracellular side. Left: Close-up view of Arg24 in helix 1 of MtTMEM175, showing the interaction with His77 and Asp30 of the adjacent subunit. The $2F_o$-F_c electron density is shown as blue mesh (at 2.4 Å, contoured at 1.8 σ, sharpened with b=-25). Right: Negative difference electron density in the structure of CmTMEM175 at the position of Arg12. The $2F_o$-F_c electron density (at 3.3 Å, contoured at 1.55 σ, blue) and the F_o-F_c density (contoured at -3 σ, red) are depicted. **h,** Defective tetramer assembly. Left: Size exclusion chromatograms from a Superdex 200 5/150 column of MtTMEM175 Arg24 mutant proteins compared to a WT chromatogram. Right: Coomassie-stained SDS-PAGE gel of purified R24A and R24K mutant proteins that were subjected to SEC.

Figure 1–figure supplement 2 | Electron density map of MtTMEM175 transmembrane helices

Electron density map in helices 1-6 with the model superimposed. Selected residues are labelled. The $2F_o$-F_c density (at 2.4 Å, contoured at 1.5-1.8 σ after sharpening with b=-25, blue) is displayed.

Figure 1–figure supplement 3 | Electron density map of MtTMEM175

Electron density map at various regions with the model superimposed. Selected residues are labelled. **a,** K^+ hydrate ($1K^+$) and surrounding. **b,** $2K^+$ and surrounding. **c,** A section of helix 1 showing the electron density for Thr38. **d,** Hydrogen-bond network in helices 1-3. The view is from the extracellular side. **e,** Interactions of maltose with MBP. The $2F_o$-F_c density (at 2.4 Å, contoured at 1.8-2.0 σ after sharpening with b=-25, blue) is displayed.

Figure 1–figure supplement 4 | Plots of I/sigI vs. resolution

Plots of I/sigI vs. resolution for the different crystallographic data sets. **a,** Native. **b,** Potassium/ Sulfur. **c,** Cesium. **d,** Rubidium. **e,** Zinc. **f,** T38A_Native. **g,** T38A_Zinc. A black box in the small insets marks the zoomed main panels at high resolution.

Figure 2–figure supplement 1 | K^+ selectivity in ScTMEM175 and electron density of a putative maltoside in the MtTMEM175 structure

a, Current responses of ScTMEM175 transfected HEK293 cells to voltage steps between ±100 mV (left). Cells were measured with 150 mM Na^+ and 150 mM K^+ in the bath and pipette solution, respectively. Mean steady state I/V relation (±s.d.) from 4 cells measured under the same condition. Data were

normalized to currents at +100 mV. The mean reversal voltage of the 4 cells is -37±9 mV (right). **b,** Residual density on the extracellular entrance of MtTMEM175 was attributed to a detergent molecule (DDM or DM). The $2F_o$-F_c density (at 2.4 Å, contoured at 1.5 σ after sharpening with b=-40, blue) is displayed. Only one subunit is shown. **c,** Close-up views on the maltoside with overlaid $2F_o$-F_c density. **d,** Current responses of HEK293 cells expressing MtTMEM175 to voltage steps from 0 mV to +80/-100 mV before (black) and after (red) adding 10 mM maltose to the bath solution with 150 mM Na^+.

Figure 2–figure supplement 2 | Plasma membrane localization of TMEM175 proteins

a, Expression profile of C-terminally vYFP-tagged MtTMEM175 in HEK293 cells. **b,** TIRF images of membrane patches from decapitated HEK293 cells. Patches were obtained from cells transiently expressing C-terminally vYFP-tagged hTMEM175 (A), MtTMEM175 (B) or MtTMEM175 T38A mutant (C). Untransfected cells served as a negative control (D). Columns from left to right: ER stained with ER tracker blue, plasma membrane (PM) stained red with CMDR, vYFP-tagged TMEM175 proteins. Last column shows merged images of different vYFP-tagged TMEM175 variants with ER and PM stain. Scale bar = 2 µm.

Figure 2–figure supplement 3 | Cell surface labelling of MtTMEM175 using Nb_{51H01}-vYFP

a, SDS Page of purified vYFP-tagged Nb_{51H01} before application in (b,c,f). **b,c,f,** Bright field (top row) and GFP-channel images (bottom row) after application of purified Nb_{51H01}-vYFP to MOCK (b) or MtTMEM175 (c,f) transfected HEK cells. **d,e,** Enlarged sections of epifluorescence images in (c). In (f) the Nb_{51H01}-vYFP was pre-absorbed with an excess of purified non-fluorescent MtTMEM175 before application to the cells.

Figure 2–figure supplement 4 | Purification of MtTMEM175 from HEK cells

a, Coomassie stained SDS-PAGE of purified MtTMEM175 from HEK cells before subjecting to size exclusion chromatography in (b). **b,** Size exclusion chromatography with MtTMEM175 purified from HEK cells (blue) in comparison with MtTMEM175 purified from *E.coli* (red). The difference in the retention volumes between the two samples arises from the presence (blue) or absence (red) of the purification tags. The peak heights are normalized.

Figure 3–figure supplement 1 | K^+ coordination in MtTMEM175, 3_{10}-helix in CmTMEM175 and analysis of the ion binding site region in CmTMEM175

a-b, Anomalous difference electron density measured at 2.02460 Å in crystals of MtTMEM175. **a,** Verification of K^+ ions at positions $1K^+$ at the extracellular entrance and $2K^+$ within the pore close to the intracellular entrance. The anomalous difference density map at +3 σ is shown as green mesh (at 3.5 Å, blurred with b=165). For comparison, the $2F_o$-F_c electron density from the best dataset (at 2.4 Å, contoured at 1.8 σ, sharpened with b=-25) is illustrated as blue mesh at the respective positions of $1K^+$ and $2K^+$. In (b), all methionine and cysteine positions are shown. **c,d,** Geometry and dimensions of the hydrated K^+ in MtTMEM175. Angles and atom-to-atom distances are indicated in degrees (°) and Å, respectively. **e,** Coordination of K^+ in KcsA by backbone oxygens (left, 1K4C, S2 position) and geometry of a hydrated K^+ ion in the KcsA vestibule in proximity to the selectivity filter (right, 1K4C). **f,** Extracellular tips of helix 1 in CmTMEM175 (cyan) and MtTMEM175 (orange) shown as stick/cartoon representation.

Only backbone atoms are displayed. In MtTMEM175 four residues complete a helical turn (alpha helical) while in CmTMEM175 three residues complete a helical turn (3_{10}-helix). **g,h,** The loop following the 3_{10}-helix in CmTMEM175 is colored in green and participates in the formation of crystal contacts (h). Reference residues are displayed in a sequence alignment in (g)**. i,k,** Superposition of the extracellular ends of helix 1 in MtTMEM175 and CmTMEM175 with approximate deviations indicated in Å (side and top view of the ion binding site). Thr38 and Leu35 (MtTMEM175, orange) were aligned with corresponding Thr26 and Ile23 (CmTMEM175, cyan). Only main chain atoms are shown. The K^+ hydrate from the MtTMEM175 structure is shown as spheres.

Figure 4–figure supplement 1 | Conservation in TMEM175 proteins

a-d, Conservation in TMEM175 projected onto the structure of MtTMEM175 (using AL2CO). Highly conserved residues are indicated and labelled. In (a) and (b), a side view is shown and one subunit has been omitted for clarity. **c,d,** View from the intracellular side into the pore. Key residues are shown and pore-lining Leu35 is displayed for orientation. **e,** Sequence alignment of helix 1. A BLAST search within the prokaryotic phyla was done using the sequence of hTMEM175 as query and the first 100 hits were aligned against each other. The conservation between helix 1 of the bacterial homologs with helix 1 of MtTMEM175 (top sequence) and hTMEM175 (repeat 2, bottom sequence) is given in percent in a bar chart. Conserved residues between MtTMEM175 and hTMEM175 are marked in grey. Color coding in the alignment is as in Figure 1–figure supplement 1d.

Figure 5–figure supplement 1 | Threonine 38 in MtTMEM175, threonine and serine residues in the pore of MtTMEM175 and hTMEM175

a,b, Position of the highly conserved Thr38 in the tetramer. Side view on the pore-forming helices (a) and close-up view of the bifurcated hydrogen bond between Thr38 and Ala34 (b). The $2F_o$-F_c density (at 2.4 Å, contoured at 1.8 σ after sharpening with b=-25, blue) is displayed. Distances between carbonyl oxygens and hydrogens are given in Å. **c, d,** Overlay of mutant T38A and WT MtTMEM175 structures (c) and close-up view on helix 1 (d). Only one subunit is shown. Key residues Thr38/ T38A are indicated. The $2F_o$-F_c density of WT (as in (b)) and of the T38A mutant (at 3.4 Å, contoured at 1.3 σ, grey) are shown. **e, f**, Layers comprising selectivity in MtTMEM175 (e) and hTMEM175 (f) with key residues colored in cyan and blue. Front subunit is omitted for clarity.

Figure 6–figure supplement 1 | Sensitivity to Zn^{2+} and anomalous density of Zn in the pore of MtTMEM175

a, Representative currents elicited by a ramp protocol (-80 to +40 mV in 200 ms) in HEK293 cells transfected with the MtTMEM175 T38A mutant in absence (black) and presence (red) of 5 mM $ZnSO_4$ in external bath solution containing 150 mM K^+. Column summarizes average inhibition (±s.d.) of current amplitudes at -60 mV from 4 recordings in the MtTMEM175 T38A mutant and WT, respectively. **b,** Location of zinc ions within the pore of MtTMEM175. Anomalous difference electron density of Zn^{2+} is illustrated as cyan mesh (at 2.88 Å, contoured at 4 σ, blurred with b=200). Front and rear subunits are omitted for clarity. **c,** No zinc ions can be detected in the T38A mutant of MtTMEM175 (F_o-F_c density at 3.2 Å, contoured at 4 σ (left) or at 2 σ (right), respectively, blurred with b=200).

Figure 6–figure supplement 2 | Constriction points in MtTMEM175 and CmTMEM175
a, Overlay of helix 1 from MtTMEM175 (orange) and CmTMEM175 (5VRE, cyan) with close-up view on residues Leu35, Leu39 and Leu42 in MtTMEM175 and Ile23, Leu27 and Leu30 in CmTMEM175, respectively. Deviations between the side chains and backbone oxygens of Leu42 in MtTMEM175 and Leu30 in CmTMEM175 are shown in Å. The view is from the side. **b,** The corresponding $2F_o$-F_c densities are shown for MtTMEM175 (left, at 2.4 Å, contoured at 1.8 σ after sharpening with b=-25) and CmTMEM175 (right, at 3.3 Å, contoured at 1.55 σ). A sequence alignment of helix 1 in MtTMEM175 and CmTMEM175 with the respective residues numbered is displayed. **c,** Comparison of a HOLE analysis of the pore in MtTMEM175 and CmTMEM175. The pore radius along the central axis is shown in Å. Dashed lines indicate the radii for K^+ and Na^+ without inner hydration shell. The structures used in the HOLE analysis were aligned to superimpose Leu35 and Thr38 in MtTMEM175 with Ile23 and Thr26 in CmTMEM175. d, HOLE calculation of MtTMEM175 WT and the mutant L35A. Leu35 corresponds to Ile23 in CmTMEM175. The pore radius along the central axis is shown in Å. Dashed lines indicate the radii for K^+ and Na^+ without inner hydration shell.

Supplementary table 1. Crystallographic data collection and refinement statistics. The resolution cutoff was determined by $CC_{1/2}$ criterion. For the native data set seven datasets from a single crystal were merged together. For the K^+/S data set, two sets from a single crystal have been merged together. For the Cs^+ dataset, three datasets from three crystals have been merged together. Six data sets from two crystals have been merged together for the Rb^+ data set. For the Zn^{2+} data set, two data sets from two crystals have been merged together.

Supplementary table 2. Crystallographic data collection and refinement statistics. The resolution cutoff was determined by $CC_{1/2}$ criterion. For the datasets of the T38A mutant and the T38A mutant soaked with Zn^{2+}, four datasets from two crystals have been merged together each.

References:

1. Xinghua, F., Zhuangzhuang, Z., Qian, L. & Zhiyong, T. Lysosomal potassium channels: Potential roles in lysosomal function and neurodegenerative diseases. *CNS & Neurological Disorders - Drug Targets* **17**, 261-266 (2018).
2. Perera, R.M. & Zoncu, R. The lysosome as a regulatory hub. *Annual Review of Cell and Developmental Biology* **32**, 223-253 (2016).
3. Lamming, D.W. & Bar-Peled, L. Lysosome: The metabolic signaling hub. *Traffic* **20**, 27-38 (2019).

4. Li, P., Gu, M. & Xu, H. Lysosomal ion channels as decoders of cellular signals. *Trends in Biochemical Sciences* **44**, 110-124 (2019).
5. Henning, R. pH gradient across the lysosomal membrane generated by selective cation permeability and Donnan equilibrium. *Biochimica et Biophysica Acta (BBA) - Biomembranes* **401**, 307-316 (1975).
6. Cang, C., Aranda, K., Seo, Y.-j., Gasnier, B. & Ren, D. TMEM175 is an organelle K^+ channel regulating lysosomal function. *Cell* **162**, 1101-1112 (2015).
7. Lee, C. et al. The lysosomal potassium channel TMEM175 adopts a novel tetrameric architecture. *Nature* **547**, 472-475 (2017).
8. Jinn, S. et al. TMEM175 deficiency impairs lysosomal and mitochondrial function and increases α-synuclein aggregation. *Proceedings of the National Academy of Sciences of the United States of America* **114**, 2389-2394 (2017).
9. Nalls, M.A. et al. Large-scale meta-analysis of genome-wide association data identifies six new risk loci for Parkinson's disease. *Nature Genetics* **46**, 989-993 (2014).
10. Chang, D. et al. A meta-analysis of genome-wide association studies identifies 17 new Parkinson's disease risk loci. *Nature Genetics* **49**, 1511-1516 (2017).
11. Su, M. et al. Structural basis for conductance through TRIC cation channels. *Nature Communications* **8**, 15103 (2017).
12. Doyle, D.A. et al. The structure of the potassium channel: Molecular basis of K^+ conduction and selectivity. *Science* **280**, 69-77 (1998).
13. Laverty, D. et al. Cryo-EM structure of the human α1β3γ2 GABA(A) receptor in a lipid bilayer. *Nature* **565**, 516-520 (2019).
14. Biel, S. et al. Mutation in S6 domain of HCN4 channel in patient with suspected Brugada syndrome modifies channel function. *Pflügers Archiv - European Journal of Physiology* **468**, 1663-1671 (2016).
15. Chen, Q. et al. Structure of mammalian endolysosomal TRPML1 channel in nanodiscs. *Nature* **550**, 415-418 (2017).
16. Guo, J. et al. Structures of the calcium-activated non-selective cation channel TRPM4. *Nature* **552**, 205-209 (2017).
17. Shen, P.S. et al. The structure of the polycystic kidney disease channel PKD2 in lipid nanodiscs. *Cell* **167**, 763-773 (2016).
18. Zhou, Y., Morais-Cabral, J.H., Kaufman, A. & MacKinnon, R. Chemistry of ion coordination and hydration revealed by a K^+ channel–Fab complex at 2.0 Å resolution. *Nature* **414**, 43-48 (2001).
19. Alam, A. & Jiang, Y. High resolution structure of the open NaK channel. *Nature Structural & Molecular Biology* **16**, 30-34 (2009).
20. McGoldrick, L.L. et al. Opening of the human epithelial calcium channel TRPV6. *Nature* **553**, 233-237 (2018).
21. Zhou, Y. & MacKinnon, R. The occupancy of ions in the K^+ selectivity filter: Charge balance and coupling of ion binding to a protein conformational change underlie high conduction rates. *Journal of Molecular Biology* **333**, 965-975 (2003).
22. Zhou, M. & MacKinnon, R. A mutant KcsA K^+ channel with altered conduction properties and selectivity filter ion distribution. *Journal of Molecular Biology* **338**, 839-846 (2004).

23. Krishnan, M.N., Trombley, P. & Moczydlowski, E.G. Thermal stability of the K^+ channel tetramer: Cation interactions and the conserved threonine residue at the innermost site (S4) of the KcsA selectivity filter. *Biochemistry* **47**, 5354-5367 (2008).
24. Chatelain, F.C. et al. Selection of inhibitor-resistant viral potassium channels identifies a selectivity filter site that affects barium and amantadine block. *PLoS ONE* **4**, e7496 (2009).
25. Derebe, M.G. et al. Tuning the ion selectivity of tetrameric cation channels by changing the number of ion binding sites. *Proceedings of the National Academy of Sciences of the United States of America* **108**, 598-602 (2011).
26. Sauer, D.B., Zeng, W., Canty, J., Lam, Y. & Jiang, Y. Sodium and potassium competition in potassium-selective and non-selective channels. *Nature Communications* **4**, 2721 (2013).
27. Kast, S.M., Kloss, T., Tayefeh, S. & Thiel, G. A minimalist model for ion partitioning and competition in a K^+ channel selectivity filter. *The Journal of General Physiology* **138**, 371-373 (2011).
28. Lee, C.-H. & MacKinnon, R. Structures of the human HCN1 hyperpolarization-activated channel. *Cell* **168**, 111-120 (2017).
29. Alam, A. & Jiang, Y. Structural analysis of ion selectivity in the NaK channel. *Nature Structural & Molecular Biology* **16**, 35-41 (2009).
30. Gouaux, E. & MacKinnon, R. Principles of selective ion transport in channels and pumps. *Science* **310**, 1461-1465 (2005).
31. Jinn, S. et al. Functionalization of the TMEM175 p.M393T variant as a risk factor for Parkinson disease. *Human Molecular Genetics* (2019).
32. Hilf, R.J.C. et al. Structural basis of open channel block in a prokaryotic pentameric ligand-gated ion channel. *Nature Structural & Molecular Biology* **17**, 1330-1336 (2010).
33. Vieira-Pires, R.S. & Morais-Cabral, J.H. 3_{10} helices in channels and other membrane proteins. *The Journal of General Physiology* **136**, 585-592 (2010).
34. Yang, T. et al. Structure and selectivity in bestrophin ion channels. *Science* **346**, 355-359 (2014).
35. Dickson, V.K., Pedi, L. & Long, S.B. Structure and insights into the function of a Ca^{2+}-activated Cl^- channel. *Nature* **516**, 213-218 (2014).
36. Vaisey, G., Miller, A.N. & Long, S.B. Distinct regions that control ion selectivity and calcium-dependent activation in the bestrophin ion channel. *Proceedings of the National Academy of Sciences of the United States of America* **113**, E7399-E7408 (2016).
37. Rao, S., Klesse, G., Stansfeld, P.J., Tucker, S.J. & Sansom, M.S.P. A BEST example of channel structure annotation by molecular simulation. *Channels* **11**, 347-353 (2017).
38. Miller, A.N., Vaisey, G. & Long, S.B. Molecular mechanisms of gating in the calcium-activated chloride channel bestrophin. *eLife* **8**, e43231 (2019).
39. Rao, S. et al. Water and hydrophobic gates in ion channels and nanopores. *Faraday Discussions* (2018).
40. Aryal, P., Abd-Wahab, F., Bucci, G., Sansom, M.S.P. & Tucker, S.J. A hydrophobic barrier deep within the inner pore of the TWIK-1 K2P potassium channel. *Nature Communications* **5**, 4377 (2014).

Methods

Reagent type (species) or resource	**Designation**	**Source or reference**	**Identifiers**
Gene (*Marivirga tractuosa)*	MtTMEM175	DSM 4126	E4TN31
Gene (*Homo sapiens*)	hTMEM175	Sourcebioscience	Q9BSA9, IRAUp969F1019D
Gene (*Streptomyces collinus*)	scTMEM175	Synthesized by GenScript	S5VBU1
Recombinant DNA reagent	pBXC3H	Dutzler lab	Addgene # 47068
Recombinant DNA reagent	pcDXC3M	Dutzler lab	Addgene #49030
Recombinant DNA reagent	pcDXC3GMS	Dutzler lab	Addgene #49031
Recombinant DNA reagent	pBXNPHM3	Dutzler lab	Addgene #110099
Cell line (*Homo sapiens*)	HEK293	Germ. Collection Microorg. & cell cultures, Braunschweig	ACC 305, tested mycoplasma negative
Strain, strain background (*Escherichia coli*)	MC1061	Dutzler lab	Made by Malcolm Casadaban https://cgsc.biology.yale.edu/Strain.php?ID=11225
Commercial assay or kit	Superdex 200 10/300	GE healthcare	Cat#17517501
Commercial assay or kit	Pierce™ Streptavidin Plus UltraLink™ resin	Thermo Fisher Scientific	Cat#53117

Commercial assay or kit	Ni-NTA resin	Qiagen	Cat#30230
Commercial assay or kit	Superdex 200 5/150 increase	GE healthcare	Cat#28990945
Commercial assay or kit	Strep-Tactin® Superflow® high capacity 50% suspension	Iba lifesciences	Cat#2-1208-010
Chemical compound, drug	cOmplete, EDTA-free Protease Inhibitor Cocktail	Roche	Cat#5056489001
Chemical compound, drug	n-dodecyl-β-d-maltopyranoside, Solgrade	Anatrace	Cat#D310S
Chemical compound, drug	n-decyl-β-d-maltopyranoside, Solgrade	Anatrace	Cat#D322S
Chemical compound, drug	Desthiobiotin	Iba lifesciences	Cat#2-1000-002
Chemical compound, drug	*E.coli* polar lipids	Avanti polar lipids	Cat#100600
Chemical compound, drug	Fugene	Promega	Cat#E2311
Chemical compound, drug	CellMask™ Deep Red	Thermo Fisher	Cat#C10046
Chemical compound, drug	ER-tracker™ Blue-white DPX	Thermo Fisher	Cat#E12353
Chemical compound, drug	Accutase	Thermo Fischer	Cat#A1110501

Chemical compound, drug	Dulbecco's modified Eagle's medium	Thermo Fischer	Cat#0685G and Cat#D5671
Chemical compound, drug	L-Glutamine	Sigma	Cat#G7513
Chemical compound, drug	GeneJuice Transfection Reagent	Millipore Corp	Cat#70967-5
Chemical compound, drug	Fetal bovine serum (FBS)	Sigma	Cat#BCBV7601 and Cat#F7524
Other	EPC-9 Amplifier	Heka Electronics	
Software, algorithm	Fiji	Schindelin et al 2019	http:://imagej.net/Fiji
Software, algorithm	PulseFit	Heka Electronics	
Software, algorithm	PatchMaster V2x90,3	Heka Electronics	
Software, algorithm	FitMaster V2x90,1	Heka Electronics	
Software, algorithm	IGOR version 6.3.7.2	WaveMetrics	
Software, algorithm	JPCalcWin version 1.01	https://medicalsciences.med.unsw.edu.au/research/research-services/ies/jpcalcwin	

Cloning

Thirty TMEM175 genes were cloned from genomic DNA of various eubacteria. The genes were flanked by a 3C protease cleavage site, a myc-tag and a StrepTagII, either on the N- or C-terminus. The TMEM175 gene of *Marivirga tractuosa* (UniProt accession # E4TN31) was cloned from the strain DSM 4126. The TMEM175 cDNA of *Streptomyces collinus* (UniProt accession # S5VBU1) was synthesized by GenScript. For expression in MC1061 *E. coli*, TMEM175 genes were expressed from the FX-cloning plasmid pBXC3H [41] (Addgene # 47068) with a stop codon. For electrophysiology and expression in

HEK293 cells, the TMEM175 genes were cloned without tags into the plasmids pcDXC3MS [42,43] (Addgene #49030) followed by a stop-codon as well as into the vector pcDXC3GMS [42,43] (Addgene #49031) (where EGFP was replaced by Venus-YFP (vYFP) using the *KpnI* sites) to obtain a C-terminally vYFP tagged channel. Both, tagged and untagged versions yielded similar results. For TIRF microscopy the TMEM175 genes were cloned into the vector pcDXC3GMS [42,43] (Addgene #49031) to produce a fusion to vYFP. For cell surface labeling of MtTMEM175 with Nb51H01 and for size exclusion profiles of MtTMEM175 expressed in HEK cells, MtTMEM175 was cloned into pcDXC3MS [42,43] (Addgene #49030) to include a streptavidin binding peptide tag for purification (SBP) [44]. Nb_{51H01} was cloned into pcDXC3GMS (Addgene #49031) to include a vYFP tag in addition to the purification tag. For the selection of nanobodies, the MtTMEM175 gene was cloned into pBXC3H to purify the protein using a deca- histidine tag. An Avi-Tag for biotinylation was introduced by PCR preceding the histidine tag at the C-terminus. Positive nanobodies were subcloned into the plasmid pBXNPHM3 [43,45,46] (Addgene #110099) for expression. C-terminally MBP (malE, *Escherichia coli K12*) tagged versions of nanobodies were generated by cloning nanobody genes and N-terminally truncated MBP genes into pBXNPHM3. The last four amino acids of MBP (RITK) were replaced with PG. The resulting expression construct consists of a nanobody, a valine linker that connects the N-terminally truncated MBP, preceded by the pelB leader sequence, a deca- histidine tag, an MBP and a 3C protease cleavage site as depicted in Figure 1–figure supplement 1b. Mutant proteins were generated by site directed mutagenesis. All constructs were verified by Sanger sequencing.

Cell culture and transfection protocol

Membrane currents were recorded from HEK cells transiently expressing TMEM175 proteins. For this low passage human embryonic kidney (HEK293) cells were cultured in Dulbecco's modified Eagle's medium (Merck) supplemented with 10% fetal bovine serum (Euroclone), 100 IU/mL of penicillin, 100 µg/ml of streptomycin, and stored in a 37 °C humidified incubator with 5% CO_2. Transfections were performed with GeneJuice Transfection Reagent (Millipore Corp) according the producer protocol: The MtTMEM175 genes inserted in pcDXC3MS [42,43] were co-transfected with a plasmid containing green fluorescent protein (GFP) and incubated in dark. Human TMEM175 constructs were cloned into pcDXC3GMS [42,43] with a C-terminal vYFP tag.

Patch clamp recordings

One to two days after transfection, cells were dispersed by accutase treatment and seeded on 35-mm plastic petri dishes (on 15-mm cover slips) to allow single cell measurements. Green fluorescent cells were selected for patch clamp measurements. Membrane currents were recorded in whole cell configuration using an EPC9 or EPC10 patch-clamp amplifier (HEKA Electronics) controlled by the PatchMaster software (HEKA). Micropipettes with a resistance of about 2 MΩ were made from 1.5 mm thin-walled glass and fire-polished. The pipette solution contained (in mM) 150 KOH, 5 HCl, 10 HEPES, pH 7.4, titrated with methanesulfonic acid. The standard bath solution contained (in mM) 150 KOH, 1 $CaCl_2$, 1 $MgCl_2$, 10 TEA, 10 HEPES/KOH, pH 7.4, titrated with methanesulfonic acid. For measurements of selectivity K^+ was replaced by other cations of interest. Relevant liquid junction voltages were calculated with JPCalcWin (UNSW Sydney). Differences in osmolarity between pipette and bath solution were compensated by D-mannitol. Membrane currents were either measured by voltage step- or ramp protocols. In standard step protocol the cell was clamped for 200 ms in 20 mV steps from holding voltage (0 mV, 100 ms) to test voltages between ±100 mV before returning to holding voltage (100 ms). The steady state current at the test voltages was measured during the final 20 ms of clamp steps. In ramp protocols the voltage increased from a holding voltage (-80 mV, 20 ms) in 200 ms to +40 mV (20 ms).

Expression and purification of MtTMEM175 from *E.coli*

MC1061 *E.coli* cells harboring the C-terminally tagged MtTMEM175 gene were grown in terrific broth with 100 µg/ml ampicillin to an OD_{600} of 0.5 at 37°C. Expression was induced with 0.02% Arabinose and continued over night at 18°C. Cells were harvested and resuspended in 150 mM NaCl, 50 mM Hepes-NaOH pH 7.6, 10% glycerol containing protease inhibitors (Complete, Roche), DNase I and 5 mM $MgCl_2$. Cells were lysed at 15000-25000 p.s.i. Cell debris was removed by centrifugation at 8000g for 30 minutes. Membranes in the supernatant were harvested by centrifugation using a 45 TI rotor (Beckmann) at 42000 r.p.m. for 1 h and resuspended in 250 mM KCl, 20 mM Hepes-NaOH pH 7.6, 15% glycerol. Extraction of the protein was carried out using 2% *n*-dodecyl-β-d-maltopyranoside (DDM, Anatrace) and protease inhibitors (Roche) for 1 h and subsequently centrifuged at 42000 r.p.m. using a 45 Ti rotor (Beckmann). The supernatant was incubated in batch with Strep-Tactin resin (Strep-Tactin Superflow high capacity, iba/Göttingen) for 1 h, washed with 150 mM KCl, 10 mM Hepes-NaOH pH 7.6, 10 % glycerol, 50 µg ml^{-1} *E.coli* polar lipids (Avanti) and 0.03% DDM, and MtTMEM175 was eluted with the wash buffer containing 5 mM *d*-Desthiobiotin (Sigma-Aldrich). The protein was cleaved using HRV 3C protease and concentrated to 10-20 mg/ml using Amicon concentrators (Millipore) with a 100kDa cutoff. The MtTMEM175 protein was mixed with Mb_{51H01} in a molar ratio of 2.2– 2.5. For this, concentrated

Mb_{51H01} was supplemented with 3mM maltose to keep MBP in the substrate-bound conformation and DDM was added to 0.03 %. After that, concentrated MtTMEM175 was added for complex formation. The mixture was left on ice for 30 minutes and applied to a Superdex 200 10/300 column (GE healthcare) equilibrated with 150 mM KCl, 5 mM Hepes-NaOH pH 7.6, 2.5 mM Maltose and 0.03 % DDM. The peak fractions were pooled and concentrated to 8-16 mg/ml for crystallization. All Steps were performed on ice or at 4 °C. Mutant proteins were purified in the same way.

Expression and purification of MtTMEM175 / fluorescent Nb_{51H01} from HEK293 cells

Low passage HEK293 cells were transiently transfected with MtTMEM175 (cloned into pcDXC3MS [42,43], Addgene #49030) or Nb_{51H01} (cloned into pcDXC3GMS [42,43], Addgene #49031) using Fugene following the manufacturers protocol. 40 hours after transfection, the cells were harvested. The proteins containing a streptavidin-binding peptide (SBP) tag [44] were purified using Pierce™ Streptavidin Plus UltraLink™ resin as described [42,43] but using the same buffers as described for the purification of MtTMEM175 from *E.coli* expressions, except that 5 mM *d*-desthiobiotin in the elution buffer was replaced with 3 mM biotin. Size exclusion chromatography was performed using a Superdex200 increase 5/150 column.

Multi angle laser light scattering (MALLS) measurements

3C-protease cleaved MtTMEM175 protein was purified as described above except that the peak fraction after size exclusion chromatography was diluted to 35 µM (1mg/ml) before subjecting it to MALLS-SEC using a Superdex 200 10/300 column (GE healthcare) with an Agilent LC-1100 system coupled to an Optilab rEX refractometer (Wyatt Technology) and a miniDAWN 3-angle light-scattering detector (Wyatt Technology). The SEC buffer contained 150 mM KCl, 10 mM Hepes-NaOH and 0.03 % DDM at pH 7.6 at RT. Data was analyzed with ASTRA software (Wyatt Technology).

Generation of nanobodies in Alpacas

Nanobodies against MtTMEM175 were raised in alpacas (*Vicugna pacos*) at the Nanobody Service Facility of the University of Zurich, NSF/UZH) as previously described [43]. Briefly, alpacas were immunized four times with 14-day intervals by injecting 100 µg of purified MtTMEM175 protein at a concentration of 35 µM (in 150 mM KCl, 10 mM Hepes-NaOH pH 7.6, 0.03 % DDM, 15% glycerol) subcutaneously. A blood sample was used to generate lymphocyte cDNA by reverse transcription.

946 Nanobody genes were cloned into a phagemid vector to create a phage library which was screened by
947 biopanning against biotinylated MtTMEM175 immobilized on Neutravidin-coated plates. Biotinylation
948 was performed as described using recombinant BirA enzyme [45,46]. Positive binders were identified using
949 ELISA and subcloned into pBXNPHM3 for expression.

950 **Expression and purification of nanobodies/macrobodies**

951 For expression of nanobodies in the vector pBXNPHM3, MC1061 *E. coli* cells were grown to an OD_{600} of
952 0.75 at 37°C in terrific broth containing 100 µg/ml ampicillin. Protein expression was started by addition
953 of 0.02% Arabinose and continued for 3.5 h at 37°C. Cells were harvested and resuspended in 150 mM
954 NaCl, 50 mM Tris-HCl pH 8, 20 mM imidazole, 5 mM $MgCl_2$, 10% glycerol, 10 µg/ml DNAse I and
955 protease inhibitors (Complete, Roche). Cells were lysed at 15000-25000 p.s.i. Cell debris was removed by
956 centrifugation at 42000 r.p.m in a 45 Ti rotor. The supernatant was applied in batch to NiNTA-resin for
957 1 h, washed with 150 mM KCl, 40 mM imidazole pH7.6, 10% glycerol and eluted with 150 mM KCl,
958 300 mM imidazole pH 7.6, 10% glycerol. The protein was cleaved over-night using HRV 3C protease
959 during dialysis against 150 mM KCl, 10 mM Hepes-NaOH, 20 mM imidazole, pH 7.6, 10% glycerol. The
960 MBP–His_{10}-fragment was removed by binding to NiNTA resin and the flow-through containing the
961 nanobodies was concentrated (Amicon) and applied to a Superdex 200 column (GE healthcare)
962 equilibrated in 150 mM KCl, 5 mM Hepes 7.6. The peak fractions were concentrated to 10-25 mg/ml
963 before mixing with MtTMEM175 for complex formation. Complex formation of purified nanobodies
964 with MtTMEM175 was analyzed by SEC, where Nb_{51H01} (corresponding macrobody is Mb_{51H01}) was
965 identified as a MtTMEM175 binder with a 1:1 stoichiometry. Macrobodies were expressed and purified
966 in the same way.

967 **Crystallization of the MtTMEM175-Mb_{51H01} complex**

968 Expression and monodispersity of purified TMEM175 proteins in small scale was analyzed by SDS-
969 PAGE and SEC. Several TMEM175 proteins were expressed at reasonable rates and eluted as
970 monodisperse species from SEC. Expression was scaled up and we could crystallize several homologues
971 readily. However, all of the crystallized proteins, including MtTMEM175, diffracted not beyond 20 Å,
972 even after extensive optimization of the crystallization conditions. To improve crystallization, we
973 generated nanobodies against MtTMEM175 as described above. Nb_{51H01}, identified by ELISA and SEC,
974 was used for complex formation with MtTMEM175 and this complex was subjected to crystallization.

The best crystals of this complex diffracted not beyond 10Å. To improve crystallization further we decided to fuse MBP to the C-terminus of Nb_{51H01} in order to increase possible crystal contacts and the chance for advantageous crystal lattices. We fused the Nb at the C-terminus with an N-terminally truncated MBP (starting at Lys^6 without the signal sequence) linked by a valine residue as depicted in Figure 1–figure supplement 1b. This resulted in the interfacial sequence PVTV**V***KLVIWIN* (Nb C-terminus underlined, linker in bold and MBP N-terminus in italics) and we named the construct Mb_{51H01}. A complex of Mb_{51H01} and MtTMEM175 was purified by SEC. Before subjecting the sample to SEC the mixture was left on ice for 15-30 minutes and eluted in 150 mM KCl, 5 mM Hepes-NaOH, 2.5 mM maltose and 0.03% DDM. The fractions containing the complex were concentrated to 8-16 mg/ml and subjected to crystallization trials.

Prior to crystallization the purified MtTMEM175-Mb_{51H01} complex was mixed with *E.coli* polar lipids (Avanti) and with *n*-decyl-β-d-maltopyranoside (DM, Anatrace) to a final concentration of 100 µg/ml and 0.3% respectively. Best crystals were obtained in a condition composed of 100 mM Tris-HCl pH 8.5, 150 mM NaCl, 150 mM $MgCl_2$ and 28- 30% PEG400 grown at 20°C. After 14 days, the crystals were dehydrated for 3-4 h using mother liquor with 36% PEG400, cryo-protected and flash-frozen in liquid propane or liquid nitrogen with similar results. The crystals giving the best datasets were additionally soaked in a cryo-protecting solution containing 5 mM $KPtCl_4$ followed by back-soaking in the cryo-protecting solution to get rid of excess platinum. For soaking in cesium and rubidium, 150 mM KCl in the cryo-protecting solution was replaced by 150 mM CsCl and 150 mM RbCl respectively. For the anomalous signal of zinc, crystals of MtTMEM175 WT protein were soaked for 15 minutes in a cryo-protecting solution containing 0.5 mM $ZnSO_4$ while the T38A mutant was soaked in 0.5- 2.5 mM $ZnSO_4$. The mutant MtTMEM175 with a T38A substitution was crystallized in the same condition and crystals were flash frozen in liquid nitrogen.

Data collection and structure determination

X-ray diffraction data was collected on the X06SA beamline at the Swiss Light Source (SLS) of the Paul Scherrer Institute (PSI) equipped with an EIGER 16M detector (Dectris) at 100K. Data reduction was performed using XDS [47] and XSCALE [48]. The resolution cut off was determined by $CC_{1/2}$ criterion [49]. Crystals of MtTMEM175 in complex with Mb_{51H01} belong to space group $P42_12$ (a = 131.2 Å, b = 131.2 Å, c = 132.6 Å), with a solvent content of 64%. Best diffracting crystals of MtTMEM175 WT were obtained after soaking in $KPtCl_4$, but no anomalous platinum signal was detected. For the native data set

seven datasets from a single crystal were merged together. Phases were obtained by molecular replacement in PHASER [50], using the individual atomic coordinates of MBP (PDB ID: 1ANF) [51], and the nanobody Nb60 (PDB ID: 5JQH) [52]. An initial round of model refinement was performed using REFMAC5 (CCP4 program suite) [53] [54], followed by density modification with Parrot [55] and automated model building by Buccaneer [56]. The initial model was improved by iterative cycles of manual model building in Coot [57] and refined in Buster-TNT [58], yielding excellent geometry (Ramachandran favored/outliers: = 95.9%/0.0%) and R_{work}/R_{free} values of 0.209/0.253 (Supplementary Tables 1 and 2). Potassium ion positions were verified by the anomalous signal at high wavelengths (λ = 2.02460 Å). Refinements using Buster-TNT indicated a high occupancy for K^+ at the position of $1K^+$ and lower occupancy for K^+ at $2K^+$. Thus, the presence of both, K^+ and Na^+, at $2K^+$ is possible. Native crystals were soaked with cesium, rubidium, and zinc and the respective ion position determined by the anomalous signal. The anomalous signal for cesium and rubidium ions was strong and identified their positions at the extracellular ion channel entrance (at $1K^+$). The anomalous signal for the data measured at the zinc K-edge (λ = 1.24610 Å) was weak, suggesting only partial occupancy. The MtTMEM175 model and structure factors (code 6HD8, 6HD9, 6HDA, 6HDB, 6HDC, 6SWR) have been deposited in the Protein Data Bank.

Regions not defined in the electron density include residues 1-3, 283-301 and 484-486 for the Mb_{51H01} expression construct, and residues 1-8 and 241-247 for MtTMEM175 (5.4 % in total). Residues 1-3 in the Nb correspond to the N-terminal remainder after 3C cleavage and would be GPS, and Residues 283-301 correspond to residues 166-184 in MBP (numbering without signal peptide) and residues 484-486 correlates to the end of MBP.

The program HOLE [59] was used to analyze the pore radius in the MtTMEM175 ion conduction pathway and the electrostatic potentials were calculated with the program APBS [60] with a grid spacing of 0.5 in a range of -5 to +5 kTe. Figure preparation was carried out in PyMOL (Schrödinger LLC). Maps were exported from Coot for use in PyMOL.

Projection of sequence conservation on the MtTMEM175 structure

Fifteen bacterial TMEM175 sequences were aligned: Nine bacterial sequences obtained from a BLAST search using the sequence of hTMEM175, and five randomly chosen bacterial TMEM175 sequences were aligned with MtTMEM175. The conservation index from this multiple sequence alignment was calculated

using AL2CO [61] and was then used to replace the values for the B-factors in the PDB file of MtTMEM175. Missing parts between the different sequences were assigned a value of -1 by default. More negative values as from the AL2CO conservation index output were set to -1. Conservation index was visualized in the MtTMEM175 structure using cyan-white-magenta colors and with the minimum set to -1 (least conservation, cyan) and the maximum set to 2.8 (maximal conservation, magenta). Sequences used for the alignment were: *Marivirga tractuosa, Lactobacillus rossiae, Mycobacterium sp., Humibacillus sp., Micromonospora chaiyaphumensis, Oscillatoria sp., Azospirillum brasilense, Niastella vici, Streptomyces collinus, Chryseobacterium sp., Streptacidiphilus carbonis, Fulvivirga imtechensis, Methylobacterium extorquens, Deinococcus geothermalis, Paenibacillus curdlanolyticus*.

TIRF microscopy

HEK293 cells transiently expressing vYFP-tagged TMEM175 proteins were grown on cover slips and decapitated by cold distilled water as described previously [14]. The remaining isolated plasma membrane patches on the glass cover slips were imaged on a Nikon Ti-E microscope (Nikon, Konan, Minato-ku, Tokyo, Japan) with a CFI Apo TIRF 100x objective (NA 1.49, WD 0.12 mm). For TIRF imaging the focus in the back focal plane was moved off-center by controlling the position of a mirror with a single-axis stage M-126. DG controlled by a C-863 Mercury Servo Controller (Physik Instrumente (PI), Karlsruhe, Germany). Plasma membrane patches and potential contamination of remaining cortical ER were stained with red fluorescent CellMask™ Deep Red (CMDR) and ER-tracker™ Blue-white DPX (both from Thermo Fisher) respectively. The fluorescent markers were excited/detected as follows: vYFP (488 nm/ 500 - 550 nm), ER-Tracker™ (561 nm/ 577.5 - 646.5 nm), CMDR (647 nm/ 662.5 - 799.5 nm).

Cell surface labeling of MtTMEM175 in HEK293 cells using fluorescent Nb_{51H01}

Low passage HEK293 cells were grown in µ-Slides VI 0.4 (Ibidi) and transiently transfected with plasmid encoding MtTMEM175 or mock transfected using Fugene following the manufacturer's protocol. 40 hours after transfection, the cells were washed twice with phosphate buffered saline (PBS) containing 10% fetal bovine serum (FBS) (PBS/FBS) before they were incubated with purified Nb_{51H01}-vYFP in PBS/FBS at a concentration of 10 µg/ ml for 20 minutes. Unbound Nb_{51H01}-vYFP was removed by two wash steps (PBS/FBS) before imaging using a Nikon Eclipse Ti2 epifluorescence microscope and a 40x Plan Fluor objective (Nikon) with an iXon^{EM}+ 885 EMCCD camera (Andor). For the pre-absorption experiment of Nb_{51H01}-vYFP with MtTMEM175, a 4-fold molar excess of MtTMEM175 (from

E.coli) was incubated with Nb_{51H01}-vYFP for 20 min and then applied to the cells as described for the treatment with Nb_{51H01}-vYFP alone (DDM concentration in the wells was below the cmc due to dilution).

References Methods:

1. Xinghua, F., Zhuangzhuang, Z., Qian, L. & Zhiyong, T. Lysosomal potassium channels: Potential roles in lysosomal function and neurodegenerative diseases. *CNS & Neurological Disorders - Drug Targets* **17**, 261-266 (2018).
2. Perera, R.M. & Zoncu, R. The lysosome as a regulatory hub. *Annual Review of Cell and Developmental Biology* **32**, 223-253 (2016).
3. Lamming, D.W. & Bar-Peled, L. Lysosome: The metabolic signaling hub. *Traffic* **20**, 27-38 (2019).
4. Li, P., Gu, M. & Xu, H. Lysosomal ion channels as decoders of cellular signals. *Trends in Biochemical Sciences* **44**, 110-124 (2019).
5. Henning, R. pH gradient across the lysosomal membrane generated by selective cation permeability and Donnan equilibrium. *Biochimica et Biophysica Acta (BBA) - Biomembranes* **401**, 307-316 (1975).
6. Cang, C., Aranda, K., Seo, Y.-j., Gasnier, B. & Ren, D. TMEM175 is an organelle K^+ channel regulating lysosomal function. *Cell* **162**, 1101-1112 (2015).
7. Lee, C. et al. The lysosomal potassium channel TMEM175 adopts a novel tetrameric architecture. *Nature* **547**, 472-475 (2017).
8. Jinn, S. et al. TMEM175 deficiency impairs lysosomal and mitochondrial function and increases α-synuclein aggregation. *Proceedings of the National Academy of Sciences of the United States of America* **114**, 2389-2394 (2017).
9. Nalls, M.A. et al. Large-scale meta-analysis of genome-wide association data identifies six new risk loci for Parkinson's disease. *Nature Genetics* **46**, 989-993 (2014).
10. Chang, D. et al. A meta-analysis of genome-wide association studies identifies 17 new Parkinson's disease risk loci. *Nature Genetics* **49**, 1511-1516 (2017).
11. Su, M. et al. Structural basis for conductance through TRIC cation channels. *Nature Communications* **8**, 15103 (2017).
12. Doyle, D.A. et al. The structure of the potassium channel: Molecular basis of K^+ conduction and selectivity. *Science* **280**, 69-77 (1998).
13. Laverty, D. et al. Cryo-EM structure of the human α1β3γ2 GABA(A) receptor in a lipid bilayer. *Nature* **565**, 516-520 (2019).
14. Biel, S. et al. Mutation in S6 domain of HCN4 channel in patient with suspected Brugada syndrome modifies channel function. *Pflügers Archiv - European Journal of Physiology* **468**, 1663-1671 (2016).
15. Chen, Q. et al. Structure of mammalian endolysosomal TRPML1 channel in nanodiscs. *Nature* **550**, 415-418 (2017).
16. Guo, J. et al. Structures of the calcium-activated non-selective cation channel TRPM4. *Nature* **552**, 205-209 (2017).
17. Shen, P.S. et al. The structure of the polycystic kidney disease channel PKD2 in lipid nanodiscs. *Cell* **167**, 763-773 (2016).

18. Zhou, Y., Morais-Cabral, J.H., Kaufman, A. & MacKinnon, R. Chemistry of ion coordination and hydration revealed by a K^+ channel–Fab complex at 2.0 Å resolution. *Nature* **414**, 43-48 (2001).
19. Alam, A. & Jiang, Y. High resolution structure of the open NaK channel. *Nature Structural & Molecular Biology* **16**, 30-34 (2009).
20. McGoldrick, L.L. et al. Opening of the human epithelial calcium channel TRPV6. *Nature* **553**, 233-237 (2018).
21. Zhou, Y. & MacKinnon, R. The occupancy of ions in the K^+ selectivity filter: Charge balance and coupling of ion binding to a protein conformational change underlie high conduction rates. *Journal of Molecular Biology* **333**, 965-975 (2003).
22. Zhou, M. & MacKinnon, R. A mutant KcsA K^+ channel with altered conduction properties and selectivity filter ion distribution. *Journal of Molecular Biology* **338**, 839-846 (2004).
23. Krishnan, M.N., Trombley, P. & Moczydlowski, E.G. Thermal stability of the K^+ channel tetramer: Cation interactions and the conserved threonine residue at the innermost site (S4) of the KcsA selectivity filter. *Biochemistry* **47**, 5354-5367 (2008).
24. Chatelain, F.C. et al. Selection of inhibitor-resistant viral potassium channels identifies a selectivity filter site that affects barium and amantadine block. *PLoS ONE* **4**, e7496 (2009).
25. Derebe, M.G. et al. Tuning the ion selectivity of tetrameric cation channels by changing the number of ion binding sites. *Proceedings of the National Academy of Sciences of the United States of America* **108**, 598-602 (2011).
26. Sauer, D.B., Zeng, W., Canty, J., Lam, Y. & Jiang, Y. Sodium and potassium competition in potassium-selective and non-selective channels. *Nature Communications* **4**, 2721 (2013).
27. Kast, S.M., Kloss, T., Tayefeh, S. & Thiel, G. A minimalist model for ion partitioning and competition in a K^+ channel selectivity filter. *The Journal of General Physiology* **138**, 371-373 (2011).
28. Lee, C.-H. & MacKinnon, R. Structures of the human HCN1 hyperpolarization-activated channel. *Cell* **168**, 111-120 (2017).
29. Alam, A. & Jiang, Y. Structural analysis of ion selectivity in the NaK channel. *Nature Structural & Molecular Biology* **16**, 35-41 (2009).
30. Gouaux, E. & MacKinnon, R. Principles of selective ion transport in channels and pumps. *Science* **310**, 1461-1465 (2005).
31. Jinn, S. et al. Functionalization of the TMEM175 p.M393T variant as a risk factor for Parkinson disease. *Human Molecular Genetics* (2019).
32. Hilf, R.J.C. et al. Structural basis of open channel block in a prokaryotic pentameric ligand-gated ion channel. *Nature Structural & Molecular Biology* **17**, 1330-1336 (2010).
33. Vieira-Pires, R.S. & Morais-Cabral, J.H. 3_{10} helices in channels and other membrane proteins. *The Journal of General Physiology* **136**, 585-592 (2010).
34. Yang, T. et al. Structure and selectivity in bestrophin ion channels. *Science* **346**, 355-359 (2014).
35. Dickson, V.K., Pedi, L. & Long, S.B. Structure and insights into the function of a Ca^{2+}-activated Cl^- channel. *Nature* **516**, 213-218 (2014).

36. Vaisey, G., Miller, A.N. & Long, S.B. Distinct regions that control ion selectivity and calcium-dependent activation in the bestrophin ion channel. *Proceedings of the National Academy of Sciences of the United States of America* **113**, E7399-E7408 (2016).
37. Rao, S., Klesse, G., Stansfeld, P.J., Tucker, S.J. & Sansom, M.S.P. A BEST example of channel structure annotation by molecular simulation. *Channels* **11**, 347-353 (2017).
38. Miller, A.N., Vaisey, G. & Long, S.B. Molecular mechanisms of gating in the calcium-activated chloride channel bestrophin. *eLife* **8**, e43231 (2019).
39. Rao, S. et al. Water and hydrophobic gates in ion channels and nanopores. *Faraday Discussions* (2018).
40. Aryal, P., Abd-Wahab, F., Bucci, G., Sansom, M.S.P. & Tucker, S.J. A hydrophobic barrier deep within the inner pore of the TWIK-1 K2P potassium channel. *Nature Communications* **5**, 4377 (2014).
41. Geertsma, E.R. & Dutzler, R. A versatile and efficient high-throughput cloning tool for structural biology. *Biochemistry* **50**, 3272-3278 (2011).
42. Brunner, J.D., Lim, N.K., Schenck, S., Duerst, A. & Dutzler, R. X-ray structure of a calcium-activated TMEM16 lipid scramblase. *Nature* **516**, 207-212 (2014).
43. Schenck, S. et al. Generation and characterization of anti-VGLUT nanobodies acting as inhibitors of transport. *Biochemistry* **56**, 3962-3971 (2017).
44. Keefe, A.D., Wilson, D.S., Seelig, B. & Szostak, J.W. One-step purification of recombinant proteins using a nanomolar-affinity streptavidin-binding peptide, the SBP-tag. *Protein Expression and Purification* **23**, 440-446 (2001).
45. Ehrnstorfer, I.A., Geertsma, E.R., Pardon, E., Steyaert, J. & Dutzler, R. Crystal structure of a SLC11 (NRAMP) transporter reveals the basis for transition-metal ion transport. *Nature Structural & Molecular Biology* **21**, 990-996 (2014).
46. Geertsma, E.R. et al. Structure of a prokaryotic fumarate transporter reveals the architecture of the SLC26 family. *Nature Structural & Molecular Biology* **22**, 803-808 (2015).
47. Kabsch, W. XDS. *Acta Crystallogr D Biol Crystallogr* **66**, 125-32 (2010).
48. Kabsch, W. Integration, scaling, space-group assignment and post-refinement. *Acta Crystallogr D Biol Crystallogr* **66**, 133-44 (2010).
49. Karplus, P.A. & Diederichs, K. Linking crystallographic model and data quality. *Science* **336**, 1030-3 (2012).
50. McCoy, A.J. et al. Phaser crystallographic software. *J Appl Crystallogr* **40**, 658-674 (2007).
51. Quiocho, F.A., Spurlino, J.C. & Rodseth, L.E. Extensive features of tight oligosaccharide binding revealed in high-resolution structures of the maltodextrin transport/chemosensory receptor. *Structure* **5**, 997-1015 (1997).
52. Staus, D.P. et al. Allosteric nanobodies reveal the dynamic range and diverse mechanisms of G-protein-coupled receptor activation. *Nature* **535**, 448-52 (2016).
53. Murshudov, G.N. et al. REFMAC5 for the refinement of macromolecular crystal structures. *Acta Crystallogr D Biol Crystallogr* **67**, 355-67 (2011).
54. Winn, M.D. et al. Overview of the CCP4 suite and current developments. *Acta Crystallogr D Biol Crystallogr* **67**, 235-42 (2011).
55. Cowtan, K. Recent developments in classical density modification. *Acta Crystallogr D Biol Crystallogr* **66**, 470-8 (2010).

56. Cowtan, K. The Buccaneer software for automated model building. 1. Tracing protein chains. *Acta Crystallogr D Biol Crystallogr* **62**, 1002-11 (2006).
57. Emsley, P., Lohkamp, B., Scott, W.G. & Cowtan, K. Features and development of Coot. *Acta Crystallogr D Biol Crystallogr* **66**, 486-501 (2010).
58. Blanc, E. et al. Refinement of severely incomplete structures with maximum likelihood in BUSTER-TNT. *Acta Crystallogr D Biol Crystallogr* **60**, 2210-21 (2004).
59. Smart, O.S., Goodfellow, J.M. & Wallace, B.A. The pore dimensions of gramicidin A. *Biophysical Journal* **65**, 2455-2460 (1993).
60. Baker, N.A., Sept, D., Joseph, S., Holst, M.J. & McCammon, J.A. Electrostatics of nanosystems: Application to microtubules and the ribosome. *Proceedings of the National Academy of Sciences of the United States of America* **98**, 10037-10041 (2001).
61. Pei, J. & Grishin, N. AL2CO: calculation of positional conservation in a protein sequence alignment. *Bioinformatics* **17**, 700-12 (2001).